

Notice of Copyright

This manuscript has been authored by UT-Battelle, LLC under Contract No. DE-AC05-00OR22725 with the U.S. Department of Energy. The United States Government retains and the publisher, by accepting the article for publication, acknowledges that the United States Government retains a non-exclusive, paid-up, irrevocable, world-wide license to publish or reproduce the published form of this manuscript, or allow others to do so, for United States Government purposes. The Department of Energy will provide public access to these results of federally sponsored research in accordance with the DOE Public Access Plan (<http://energy.gov/downloads/doe-public-access-plan>).

Title:

Neutron scattering in the proximate quantum spin liquid α -RuCl₃

Authors:

Arnab Banerjee^{1*}, Jiaqiang Yan², Johannes Knolle³, Craig A. Bridges⁴, Matthew B. Stone¹, Mark D. Lumsden¹, David G. Mandrus^{2,5}, David A. Tennant⁶, Roderich Moessner⁷, Stephen E. Nagler^{1*}.

Affiliations:

¹Quantum Condensed Matter Division, Oak Ridge National Laboratory, Oak Ridge, TN 37831, U.S.A.

²Material Sciences and Technology Division, Oak Ridge National Laboratory, Oak Ridge, TN, 37831, U.S.A.

³Department of Physics, Cavendish Laboratory, JJ Thomson Avenue, Cambridge CB3 0HE, U.K.

⁴Chemical Sciences Division, Oak Ridge National Laboratory, Oak Ridge, TN 37831, U.S.A.

⁵Department of Materials Science and Engineering, University of Tennessee, Knoxville, TN 37996, U.S.A.

⁶Neutron Sciences Directorate, Oak Ridge National Laboratory, Oak Ridge, TN 37831, U.S.A.

⁷Max Planck Institute for the Physics of Complex Systems, D-01187 Dresden, Germany.

*Correspondence to: banerjeea@ornl.gov, naglerse@ornl.gov

Abstract:

The Kitaev quantum spin liquid (KQSL) is an exotic emergent state of matter exhibiting Majorana Fermion and gauge flux excitations. The magnetic insulator α -RuCl₃ is thought to realize a proximate KQSL. Here, we use neutron scattering on single crystals of α -RuCl₃ to reconstruct dynamical correlations in energy-momentum space. We discover highly unusual signals, including a column of scattering over a large energy interval around the Brillouin zone center which is very stable with temperature. This finding is consistent with scattering from the Majorana excitations of a KQSL. Other, more delicate, experimental features can be transparently associated with perturbations to an ideal model. Our results encourage further study of this prototypical material and may open a window into investigating emergent magnetic Majorana fermions in correlated materials.

Main Text:

Quantum spin liquids (QSLs) are collective magnetic states that can form in the networks of atomic moments (“spins”) in materials. The spins fail to enter an ordinary static ordered state – such as a ferromagnet – as the temperature approaches zero and instead become highly entangled and fluctuate quantum mechanically (1, 2). A defining feature of QSLs, connected to their topological nature, is excitations that carry fractional quantum numbers (3, 4) - a phenomenon underpinning the physics of the fractional quantum Hall effect (5), magnetic monopoles (6), and spin-charge separation (7). Fractionalization can be seen experimentally by momentum-energy space reconstruction. Inelastic neutron scattering directly probes magnetic correlations in space and time. Our experiments discussed below provide a comprehensive image of the collective magnetic fluctuations in a topological quantum magnet.

Kitaev’s QSL (KQSL) (8-13) is the focus of intense current interest. The Kitaev model offers a unique window on spin liquid physics as its exact solubility permits a detailed analysis of its properties, including those of its fractionalized Majorana fermion and gauge flux excitations. Beyond their significance to fundamental physics, they are of particular interest as a magnetic field turns them into non-Abelian anyons, which can underpin a quantum computing architecture topologically protected against decoherence (14, 15). The Kitaev model consists of an extremely simple spin network (8, 9) with localized $S=1/2$ spins on a honeycomb lattice with interaction Hamiltonian:

$$\mathcal{H} = \sum_{\gamma, \vec{r}} \left(K^{\gamma} S_{\vec{r}}^{\gamma} S_{\vec{r}+\vec{\delta}_{\gamma}}^{\gamma} \right) \quad \dots (1)$$

for either ferromagnetic (FM) or antiferromagnetic (AF) coupling K . Here \vec{r} runs over the lattice sites, and the index γ (= x, y, z in spin space) denotes the relevant interacting spin component for the nearest neighbor bond joined by vector $\vec{\delta}_\gamma$, with Ising interaction strength K^γ (Fig. 1A).

Insulating materials comprising weakly coupled honeycomb layers of strongly spin-orbit coupled transition metal ions in edge-sharing cubic octahedra (16) are promising candidates for realizing KQSLs. These have included iridates containing Ir^{4+} (17-20), and most recently the Ru^{3+} based honeycomb magnet $\alpha\text{-RuCl}_3$ (21-26). Here we present inelastic neutron scattering on a single crystal of $\alpha\text{-RuCl}_3$, providing a complete measurement of the magnetic response function in 4-dimensional energy-momentum space. From a technical perspective, this presents a qualitative advance over polycrystalline samples studied so far (25), or single crystal Raman studies (23), which are unable to distinguish between different directions in momentum space.

A 490 mg single crystal grown via vapor transport of phase-pure $\alpha\text{-RuCl}_3$ was used (27). This crystal has a low incidence of stacking faults and exhibits a single magnetic ordering transition at $T_N=7$ K (Fig. 1B, Fig. S1). Below T_N the magnetic order is zigzag in the individual honeycomb layers, with a three-layer periodicity out of plane. The ordered moment $\langle\mu\rangle \sim 0.5 \mu_B$, is only about $1/3^{\text{rd}}$ of the net paramagnetic moment (22, 25, 26). The details of the ordering can vary in different samples depending on the precise stacking of the layers; in any case, the ordering is incidental to the 2D QSL physics of interest here.

Figure 2 contains a first set of central results. It depicts the temperature and momentum dependence of a magnetic scattering continuum for two energy ranges: 4.5 to 7.5 meV and 7.5 to 12.5 meV. The most salient feature is the robust response centered at the Γ point: it is present from low ($T=5$ K $< T_N$) all the way to high ($T=120$ K $\gg T_N$) temperatures of order of the Kitaev

coupling estimated at $K' \approx 70 - 90$ K (24, 25). On passing from below to above T_N the central portion of the scattering strengthens. The overall intensity, although weaker, is still readily visible at very high T. At all temperatures this dynamic scattering extends through a large fraction of the Brillouin zone, indicative of short-ranged liquid correlations. (See (27) and Figs. S2 and S3 for Brillouin Zone (BZ) definitions). The energy dependence of the scattering at the Γ point is illustrated in Fig. 3, A and B at temperatures below and above T_N , respectively. Above T_N , the broad scattering continuum (marked “C”) extends nearly to 15 meV, in keeping with expectations for a pure Kitaev model with $K' \approx 5.5 - 8$ meV (24, 25). Below T_N a fraction of the spectral weight shifts into sharp (i.e., energy resolution limited) spin wave (SW) peaks arising from the small zigzag ordered moments. Crucially, the 2-dimensional nature of the response is shown by the rod-like dependence on L of the scattering illustrated in Fig. 3, C and D.

Most importantly, the persistent energy continuum at the Γ point is incompatible with conventional SW physics. Indeed, Fig. 3E shows the generic low energy SW response for a zigzag ordered state. This takes the form of dispersive energy-momentum cones centered about each M point magnetic Bragg peak (Fig. 3F). In SW theory the Γ point scattering is present only at certain fixed energy values, unlike the experimentally observed broad energy column (Fig. 2 and Fig. 3F). Moreover, SW scattering at long wavelengths is strongly sensitive to cooling through T_N (25), in stark contrast to the continuum. The latter is very broad in energy and almost independent of temperature up to around 100 K ($\sim K' \gg T_N$) consistent with the thermodynamics of the Kitaev model (23, 28-30) (Γ point scattering at $T=120$ K is shown in Fig. S6D). The energy breadth and temperature dependence of the continuum are consistent with fractionalized excitations (13, 28-30).

It is an intriguing question whether extensions of spin-wave theory, for example based on a sequence of multiple spin-wave contributions (31), might be able to account for such a phenomenology. This faces technical and conceptual challenges in accounting for the temperature-dependence of the inelastic neutron scattering data. In particular, as the low-energy single-spin wave response is reconstructed upon heating through the ordering temperature, one would naturally expect this to imply a strong renormalization of the high-energy multi-spin wave signal, which is in contrast to experimental observations.

Figure 4A shows an extended zone picture of the $T = 5$ K data integrated between $E=[4.5,7.5]$ meV, symmetrized along the $(H,H,0)$ direction. In addition to the strong scattering at $H=K=0$, features are now visible near adjacent Γ points $\pm (1,1)$, showing that the continuum spectrum repeats every 2nd BZ. Additional scattering at larger Q arises from phonons. In the following we show that a Kitaev QSL description reproduces the main qualitative features of the data; in particular, the broad energy width and T -dependence of the scattering continuum, as well as its periodicity and relative orientation in the BZ, which encodes the orientational bond-dependence of the spin anisotropy in Kitaev systems.

The momentum dependence of the scattering for a pure Kitaev model at $T=0$ is exactly known (12, 13, 27, and Fig. S5). The dynamical structure factor consists of two energy dependent correlations, those for onsite, S_0 , and nearest neighbor spins, S_I (27 and Fig. S4). For simplicity we compare the scattering to calculations for an isotropic Kitaev model. Although a slightly spatially anisotropic Kitaev exchange is likely in α - RuCl_3 (22), averaging over the in-plane structural domains (26) reduces the visibility of the anisotropy in experiments. Moreover, it is not expected to have a major effect on the higher frequency portion of the collective dynamics discussed here (25). However, in a real material, the effective Hamiltonian includes non-Kitaev

terms (10) that extend the liquid correlations and, in particular, lead to the long-range order observed below T_N . To date there is no comparably reliable theory available for the response of such an extended Hamiltonian (on which, at any rate, there is not yet universal agreement for α - RuCl_3). As a first, phenomenological, attempt to account for the effect of additional terms, we consider minimally modifying the response function of the pure Kitaev model by varying the ratio of S_I/S_0 by a factor ‘ R ’ taken to be momentum independent for simplicity. As shown below, treating this ratio as an adjustable parameter yields an excellent account of the overall momentum dependence of the scattering.

Figure 4B illustrates the scattering for $R=2$ at fixed $E=1.2 K^\gamma$. This calculation captures overall extent, orientation and periodicity of the scattering in reciprocal space. A direct comparison is made in the bottom panel, Fig. 4C, showing a cut of the intensity as a function of momentum along the (H,H) direction, integrated over a narrow band around $|(K,-K)|=0$. Also shown are three model calculations for an isotropic Kitaev model at fixed $E=1.2 K^\gamma$: AF (violet), FM (green), and AF response modified using $R=2$ (red). The FM model, in the absence of any further terms in the Hamiltonian, is clearly incompatible with the data as it shows a local minimum at the Γ point. The unmodified AF Kitaev response gives a reasonable description of the data but fails to capture the full intensity variation (Figs. S5 and S6, A to C). The modified AF Kitaev response fits the data best with $R \approx 2$ indicating a relative enhancement of the spatial correlations.

The results reported here provide a unique picture of the magnetic response function of α - RuCl_3 in momentum-energy space, and demonstrate unequivocally the presence of an extended continuum of magnetic excitations centered at the Γ point. The continuum response is

incompatible with SW theory, and indeed defies any known explanation in terms of conventional dispersive spin flip, single particle, or simple dimer magnetic excitations (27, Figs. S6 and S7). Instead, the central features of the continuum are well described by the scattering for an AF KQSL; with one phenomenological fitting parameter, nearly quantitative agreement is obtained. The exact calculation of the response function of the pure Kitaev model is based on fractionalized degrees of freedom: free Majorana fermions scattering off a pair of static emergent fluxes (12, 13). In such a scattering process the demands of energy and momentum conservation impose only weak kinematic constraints. This provides a natural and intuitive picture for the experimentally observed continuum.

One feature of the data that is not well-described by a pure Kitaev model is the six-pointed star shape of the scattering in reciprocal space. However it can be shown (27 and Figs. S8 to S10) that modest amounts of additional neighbor correlation or simple perturbations based on mean-field approaches (32) away from the integrable model can yield a similar shape even in the disordered state.

The data presented here constitute an important step in developing a complete understanding of the low and high energy dynamics in α -RuCl₃. The good agreement of the continuum scattering with the simple AF KQSL is complementary to current DFT calculations relating the low-energy spin $\frac{1}{2}$ description of the material to details of the electronic structure (33, 34). Further effort is needed to converge on an explanation of the sign of the Kitaev interaction, and to determine the magnitude of additional interactions. It would be of great interest to develop a theory that describes both the low energy response of the ordered state and the broad quantum fluctuation

continuum. At the same time, the seeming proximity of the system to a true KQSL is a strong incentive for exploring the effects of doping, pressure and field to determine a full picture of the ground and excited states. With this work, a comprehensive measurement of the high-energy excitations is now available to the community in a potential proximate Kitaev material, and may open up the opportunity to investigate the magnetic version of the elusive Majorana fermions in two dimensions.

Supplementary Materials

Materials and Methods

Supplementary Text

Figs. S1 to S11

Table S1

References (35-53)

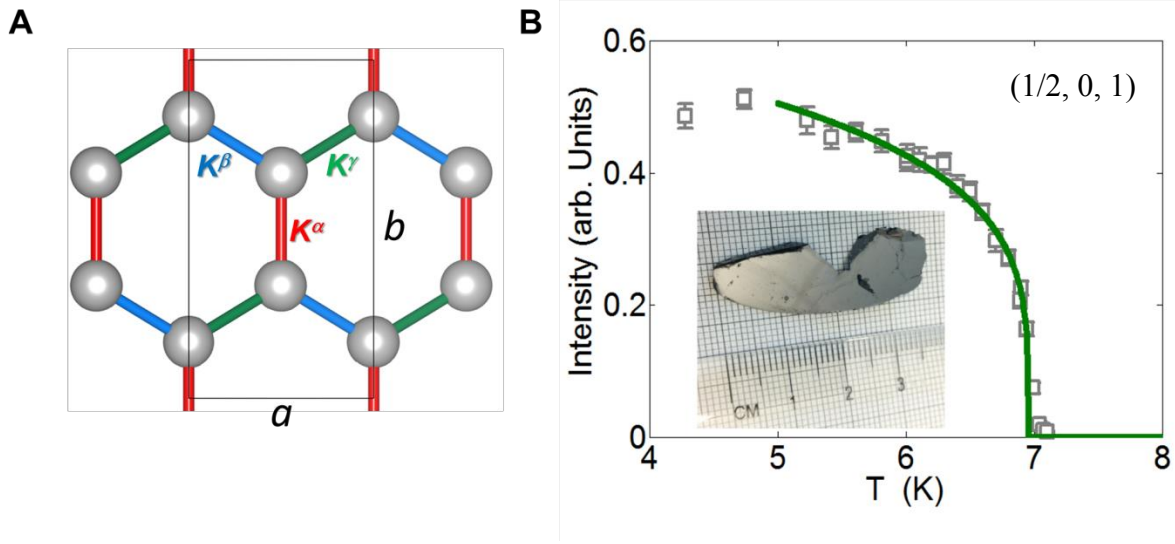


Fig. 1 Structure and magnetism in single-crystal α -RuCl₃. (A) The honeycomb lattice of Ru³⁺ magnetic ions in one plane of α -RuCl₃ showing the projections of the three mutually competing Ising bonds corresponding to the Kitaev terms in Eq. 1. (B) The intensity of the magnetic Bragg Peak occurring at the M point of the 2D honeycomb lattice corresponding to a zigzag structure with three-layer stacking ($\vec{k} = (1/2, 0, 1)/(0, 1, 1/3)$ in trigonal/monoclinic notation). The single sharp magnetic transition is characteristic of crystals with few or no stacking faults (26). The solid line is a power-law fit yielding $T_N = 6.96 \pm 0.02$ K and a critical exponent $\beta = 0.125 \pm 0.015$, suggesting 2D Ising behavior. **Inset:** The 490 mg single-crystal of α -RuCl₃ used for the neutron measurements. (For more sample details, see Materials and Methods (27)).

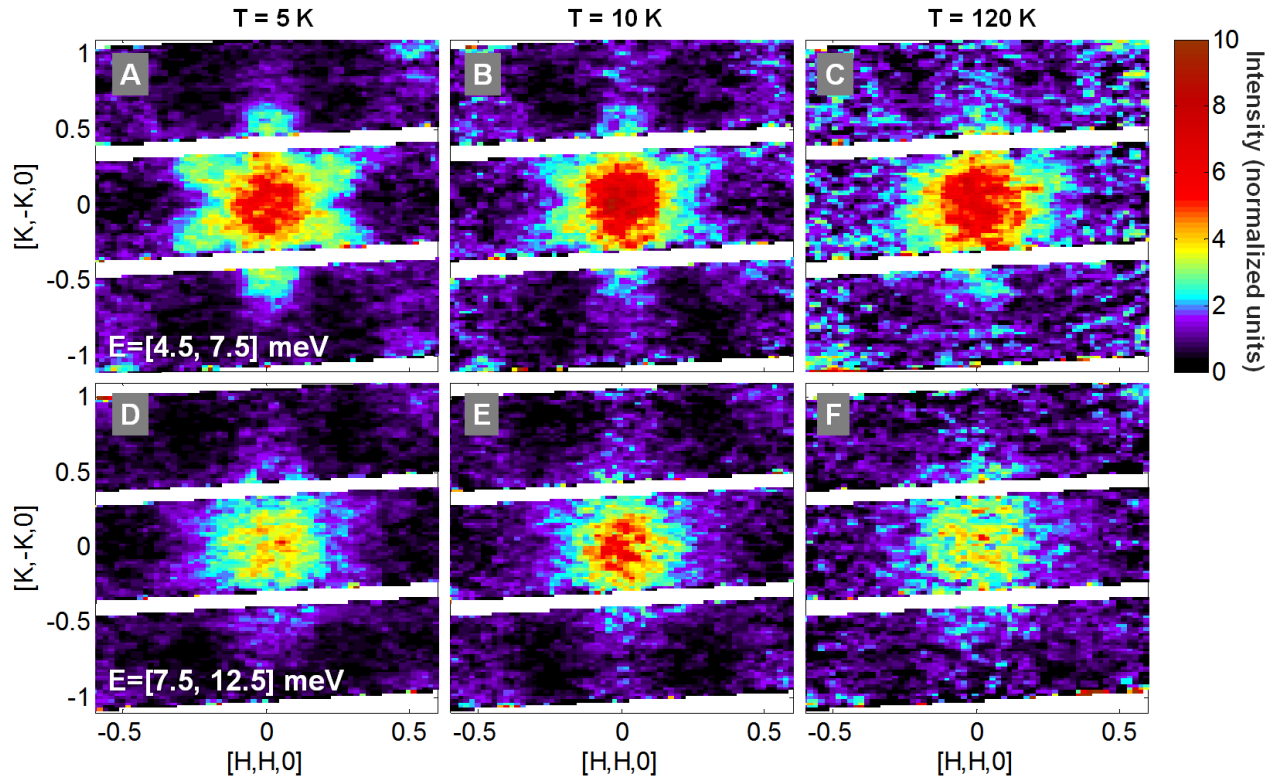


Fig. 2 Momentum and temperature dependence of the scattering continuum. Neutron scattering measurements using fixed incident energy $E_i = 40$ meV, projected on the reciprocal honeycomb plane defined by the perpendicular directions $(H,H,0)$ and $(K,-K,0)$, integrated over the interval $L=[-2.5, 2.5]$. Intensities are denoted by color as indicated in the scale at right. Measurements integrated over the energy range $[4.5, 7.5]$ meV are shown on the top row at temperatures (A) 5 K, (B) 10 K, and (C) 120 K. The corresponding measurements integrated over the interval $[7.5, 12.5]$ meV are shown in panels (D), (E), and (F). The white regions lack detector coverage. See Fig. S11 for orientationally averaged data.

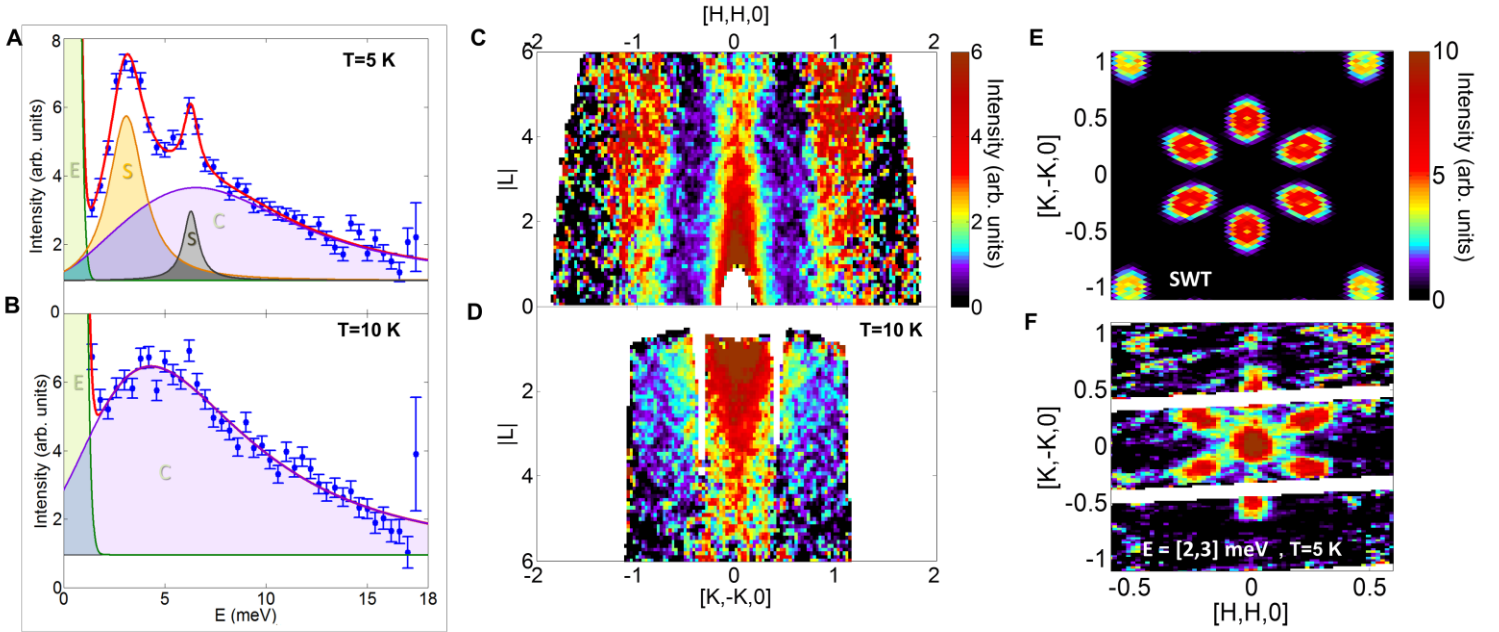


Figure 3

Fig. 3 Detailed features of the Γ point scattering. (A and B) The energy dependence of the scattering integrated over the constant momentum volume defined by the following integration ranges: $L = [-2.5, 2.5]$; $[\zeta, 0] \equiv (K, -K, 0)$ over the range $\zeta = [-\sqrt{3}/10, \sqrt{3}/10]$; $[\xi, 0] \equiv (H, H, 0)$ over the range $\xi = [-0.1, 0.1]$, at temperatures (A) 5 K, and (B) 10 K shows a broad peak. The solid lines are guides to the eye produced by modeling the elastic component as a Gaussian peak and the inelastic features using damped harmonic oscillator (DHO) functions: “E” represents an elastic component, “S” spin wave peaks appearing below T_N , and “C” the continuum. Fit parameters and the DHO function are presented in Table S1. (C) Scattering symmetrized in the (H, H, L) plane and over positive and negative L , integrated over the intervals $\zeta = [-\sqrt{3}/10, \sqrt{3}/10]$, and $E = [4.5, 7.5]$ meV at $T = 10$ K. (D) Same scattering, but in the $(K, -K, L)$ plane integrated over $\xi = [-0.1, 0.1]$ and $E = [4.5, 7.5]$ meV. (E) Representative low-energy spin wave scattering expected for a zigzag ordered phase (25). (F) Scattering at $T = 5$ K integrated over $L = [-2.5, 2.5]$ and $E = [2, 3]$ meV. The white regions lack detector coverage.

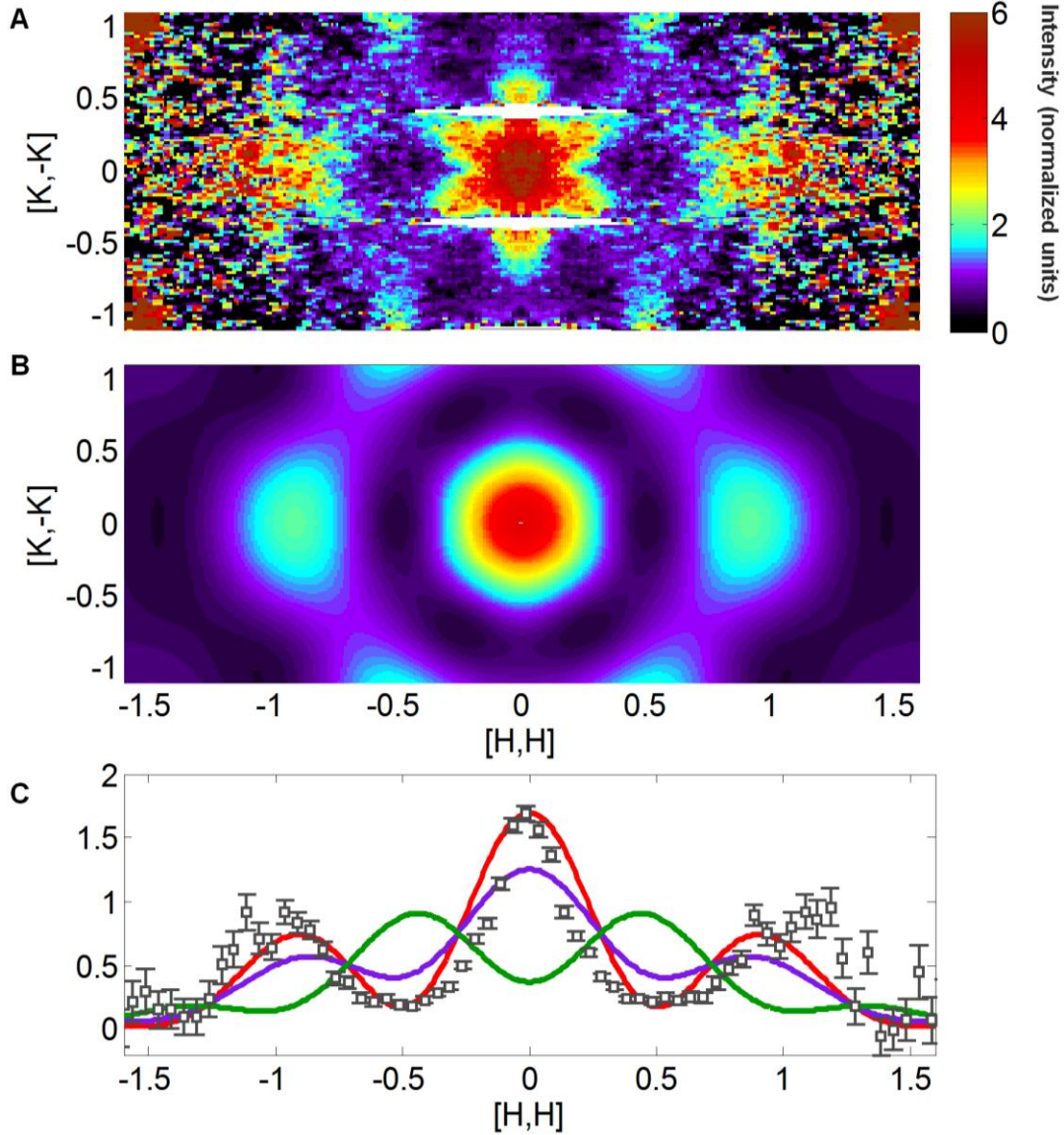


Fig. 4 Comparison of the scattering with Kitaev model calculations. (A) The data at $E_i=40$ meV, $T = 5$ K integrated over range $E = [4.5, 7.5]$ meV and $L = [-2.5, 2.5]$ and symmetrized along the (H,H) direction. (B) The expected scattering from an isotropic AF Kitaev model at an energy $E = 1.2 K\gamma$, taking into account the neutron polarization and the spherically approximated Ru^{3+} form factor. (C) Plot of the non-symmetrized data (points with error bars) along $(H,H,0)$ at $T = 5$ K, integrated over the same L and E intervals as panel A as well as $\zeta = [-\sqrt{3}/10, \sqrt{3}/10]$. The

solid red line is the calculated scattering for an AF Kitaev model with $R = 2$ as discussed in the text. The solid blue line represents the corresponding unmodified AF Kitaev model, and the green line the FM Kitaev model. Some of the scattering at larger Q near $(H,H) = \pm(1,1)$ is due to phonons.

Full reference list:

- [1] L. Balents, Spin liquids in frustrated magnets, *Nature* **464**, 199-208 (2010).
- [2] P. W. Anderson, Resonating valence bonds: A new kind of insulator? , *Mat. Res. Bull.* **8**, 153 (1973).
- [3] M. Barakshli, E. Berg, S. Kivelson, Coherent transmutation of electrons into fractionalized anyons, *Science* **346**, 722-725 (2014).
- [4] T-H. Han, J. S. Helton, S. Chu, D. G. Nocera, J. A. Rodriguez-Rivera, C. Broholm, Y. S. Lee, Fractionalized excitations in the spin-liquid state of a kagome-lattice antiferromagnet, *Nature* **492**, 406-410 (2012).
- [5] R. B. Laughlin, Anomalous Quantum Hall Effect: An Incompressible Quantum Fluid with Fractionally Charged Excitations, *Phys. Rev. Lett.* **50**, 1395 (1983).
- [6] C. Castelnovo, R. Moessner, S. L. Sondhi, Magnetic monopoles in spin ice, *Nature* **451**, 42 (2008).
- [7] Y. Jompol *et al.*, Probing Spin-Charge Separation in a Tomonaga-Luttinger Liquid, *Science* **325**, 597 (2009).
- [8] A. Kitaev, Anyons in an exactly solved model and beyond, *Annals of Phys.* **321**, 2-111 (2006).
- [9] J. G. Rau, E. K-H. Lee, H-Y Kee, Spin-Orbit Physics Giving Rise to Novel Phases in Correlated Systems: Iridates and Related Materials, *Annu. Rev. Condens. Matter Phys.* **7**, 195-221 (2015).
- [10] J. G. Rau, E. K-H. Lee, H-Y. Kee, Generic Spin Model for the Honeycomb Iridates beyond the Kitaev Limit, *Phys. Rev. Lett.* **112**, 077204 (2014).
- [11] G. Baskaran, S. Mandal, R. Shankar, Exact Results for Spin Dynamics and Fractionalization in the Kitaev Model, *Phys. Rev. Lett.* **98**, 247201 (2007).
- [12] J. Knolle, D. L. Kovrizhin, J. T. Chalker, R. Moessner, Dynamics of a Two-Dimensional Quantum Spin Liquid: Signatures of Emergent Majorana Fermions and Fluxes, *Phys. Rev. Lett.* **112**, 207203 (2014).
- [13] J. Knolle, D. L. Kovrizhin, J. T. Chalker, R. Moessner, Dynamics of fractionalization in quantum spin liquids, *Phys. Rev. B* **92**, 115127 (2015).
- [14] A.Y. Kitaev, Fault-tolerant quantum computation by anyons, *Annals of Phys.* **303**, 1 (2003).
- [15] C. Nayak, S. H. Simon, A. Stern, M. Freedman, S. D. Sarma, Non-Abelian anyons and topological quantum computation, *Rev. Mod. Phys.* **80**, 1083-1159 (2008).

- [16] G. Jackeli, G. Khaliullin, Mott Insulators in the Strong Spin-Orbit Coupling Limit: From Heisenberg to a Quantum Compass and Kitaev Models, *Phys. Rev. Lett.* **102**, 017205 (2009).
- [17] S. K. Choi, R. Coldea, A. N. Kolmogorov, T. Lancaster, I. I. Mazin, S. J. Blundell, P. G. Radaelli, Yogesh Singh, P. Gegenwart, K. R. Choi, S.-W. Cheong, P. J. Baker, C. Stock, and J. Taylor, Spin Waves and Revised Crystal Structure of Honeycomb Iridate Na_2IrO_3 , *Phys. Rev. Lett.* **108**, 127204 (2012).
- [18] S. H. Chun, J.-W. Kim, J. Kim, H. Zheng, C. C. Stoumpos, C. D. Malliakas, J. F. Mitchell, K. Mehlawat, Y. Singh, Y. Choi, T. Gog, A. Al-Zein, M. M. Sala, M. Krisch, J. Chaloupka, G. Jackeli, G. Khaliullin, B. J. Kim, Direct evidence for dominant bond-directional interactions in a honeycomb lattice iridate Na_2IrO_3 , *Nature Phys.* **11**, 462 (2015).
- [19] K. A. Modic, T. E. Smidt, I. Kimchi, N. P. Breznay, A. Biffin, S. Choi, R. D. Johnson, R. Coldea, P. Watkins-Curry, G. T. McCandless, J. Y. Chan, F. Gandara, Z. Islam, A. Vishwanath, A. Shekhter, R. D. McDonald, J. G. Analytis, Realization of a three-dimensional spin-anisotropic harmonic honeycomb iridate, *Nature Comm.* **5**, 4203 (2014).
- [20] A. Biffin, R. D. Johnson, I. Kimchi, R. Morris, A. Bombardi, J. G. Analytis, A. Vishwanath, and R. Coldea, Noncoplanar and Counterrotating Incommensurate Magnetic Order Stabilized by Kitaev Interactions in $\gamma\text{-Li}_2\text{IrO}_3$, *Phys. Rev. Lett.* **113**, 197201 (2014).
- [21] K. W. Plumb, J. P. Clancy, L. J. Sandilands, V. Vijay Shankar, Y. F. Hu, K. S. Burch, H.-Y. Kee, and Y.-J. Kim, $\alpha\text{-RuCl}_3$: A spin-orbit assisted Mott insulator on a honeycomb lattice, *Phys. Rev. B* **90**, 041112(R) (2014).
- [22] R. D. Johnson, S. C. Williams, A. A. Haghighirad, J. Singleton, V. Zapf, P. Manuel, I. I. Mazin, Y. Li, H. O. Jeschke, R. Valentí, and R. Coldea, Monoclinic crystal structure of $\alpha\text{-RuCl}_3$ and the zigzag antiferromagnetic ground state, *Phys. Rev. B* **92**, 235119 (2015).
- [23] J. Nasu, J. Knolle, D. L. Kovrizhin, Y. Motome, R. Moessner, Fermionic response from fractionalization in an insulating two-dimensional magnet, *Nature Phys.* **12**, 912-915 (2016).
- [24] L.J. Sandilands, Y. Tian, K. W. Plumb, Y.-J. Kim, and K. S. Burch, *et al.*, Scattering Continuum and Possible Fractionalized Excitations in $\alpha\text{-RuCl}_3$, *Phys. Rev. Lett.* **114**, 147201 (2015).
- [25] A. Banerjee, C. A. Bridges, J.-Q. Yan, A. A. Aczel, L. Li, M. B. Stone, G. E. Granroth, M. D. Lumsden, Y. Yiu, J. Knolle, S. Bhattacharjee, D. L. Kovrizhin, R. Moessner, D. A. Tennant, D. G. Mandrus, S. E. Nagler Proximate Kitaev quantum spin liquid behavior in a honeycomb magnet, *Nature Mat.* **15**, 733 (2016).
- [26] H. B. Cao, A. Banerjee, J.-Q. Yan, C. A. Bridges, M. D. Lumsden, D. G. Mandrus, D. A. Tennant, B. C. Chakoumakos, and S. E. Nagler, Low-temperature crystal and magnetic structure of $\alpha\text{-RuCl}_3$, *Phys. Rev. B* **93**, 134423 (2016).

- [27] See Supplementary Materials
- [28] J. Nasu, M. Udagawa, Y. Motome, Vaporization of Kitaev Spin Liquids, *Phys. Rev. Lett.* **113**, 197205 (2014).
- [29] J. Nasu, M. Udagawa, Y. Motome, Thermal fractionalization of quantum spins in a Kitaev model: Temperature-linear specific heat and coherent transport of Majorana fermions, *Phys. Rev. B* **92**, 115122 (2015).
- [30] J. Yoshitake, J. Nasu, Y. Motome, Fractional Spin Fluctuations as a Precursor of Quantum Spin Liquids: Majorana Dynamical Mean-Field Study for the Kitaev Model, *Phys. Rev. Lett.* **117**, 157203 (2016).
- [31] S.M. Winter, K. Riedl, A. Honecker, R. Valenti, Breakdown of Magnons in a Strongly Spin-Orbital Coupled Magnet, Available at arXiv:1702.08466 (2017).
- [32] D.J. Scalapino, Y. Imry, P. Pincus, Generalized Ginzburg-Landau theory of pseudo-one-dimensional systems, *Phys. Rev. B* **11**, 2042 (1975).
- [33] H-S. Kim, H-Y. Kee, Crystal structure and magnetism in α -RuCl₃: An ab initio study, *Phys. Rev. B* **93**, 155143 (2016).
- [34] S.M. Winter, Y. Li, H. O. Jeschke R. Valenti, Challenges in design of Kitaev materials: Magnetic interactions from competing energy scales, *Phys. Rev. B* **93**, 214431 (2016).
- [35] J. A. Sears, M. Songvilay, K. W. Plumb, J. P. Clancy, Y. Qiu, Y. Zhao, D. Parshall, and Y-J. Kim, Magnetic order in α -RuCl₃: A honeycomb-lattice quantum magnet with strong spin-orbit coupling, *Phys. Rev. B* **91**, 144420 (2015).
- [36] M. Majumder, M. Schmidt, H. Rosner, A. A. Tsirlin, H. Yasuoka, and M. Baenitz, Anisotropic Ru³⁺ 4d⁵ magnetism in the α -RuCl₃ honeycomb system: Susceptibility, specific heat, and zero-field NMR, *Phys. Rev. B* **91**, 180401(R) (2015).
- [37] L. Binotto, I. Pollini, G. Spinolo, Optical and Transport Properties of the Magnetic Semiconductor α -RuCl₃, *Phys. Stat. Sol. (b)* **44**, 245 (1971).
- [38] I. Pollini, Electronic properties of narrow-band material α -RuCl₃, *Phys. Rev. B* **53**, 12769 (1996).
- [39] B. H. Kim, T. Shirakawa, S. Yunoki, From a Quasimolecular Band Insulator to a Relativistic Mott Insulator in t⁵_{2g} Systems with a Honeycomb Lattice Structure, *Phys. Rev. Lett.* **117**, 187201 (2016).
- [40] A. Koitzsch, C. Habenicht, E. Müller, M. Knupfer, B. Büchner, H. C. Kandpal, J. van den Brink, D. Nowak, A. Isaeva, Th. Doert, *J_{eff}* Description of the Honeycomb Mott Insulator α -RuCl₃, *Phys. Rev. Lett.* **117**, 126403 (2016).

- [41] K. Brodersen, G. Thiele, H. Ohnsorge, I. Recke, F. Moers, Die struktur des IrBr_3 und über die ursachen der fehlordnungserscheinungen bei den in schichtenstrukturen kristallisierenden edelmetalltrihalogeniden, *J. Less-Common Mat.* **15**, 347 (1968).
- [42] M. B. Stone, J. L. Niedziela, D. L. Abernathy, L. DeBeer-Schmitt, G. Ehlers, O. Garlea, G. E. Granroth, M. Graves-Brook, A. I. Kolesnikov, A. Podlesnyak, and B. Winn, A comparison of four direct geometry time-of-flight spectrometers at the Spallation Neutron Source, *Rev. Sci. Instrum.* **85**, 045113 (2014).
- [43] G. E. Granroth, D. H. Vandergriff, S. E. Nagler, SEQUOIA: A fine resolution chopper spectrometer at the SNS, *Physica B* **385-386**, 1104-1106, (2006).
- [44] O. Arnolda, J.C. Bilheux, J.M. Borreguero, A. Buts, S.I. Campbell, L. Chapona, M. Doucet, N. Draper, R. Ferraz Leald, M.A. Gigga, V.E. Lynch, A. Markvardsen, D.J. Mikkelsone, R.L. Mikkelsone, R. Miller, K. Palmen, P. Parker, G. Passos, T.G. Perring, P.F. Peterson, S. Ren, M.A. Reuter, A.T. Savici, J.W. Taylor, R.J. Taylor, R. Tolchenov, W. Zhou, J. Zikovsky, MANTID—Data analysis and visualization package for neutron scattering and μ SR experiments, *Nuclear Instruments and Methods in Physics Research Section A: Accelerators, Spectrometers, Detectors and Associated Equipment* **764**, 156-166 (2014).
- [45] R.T. Azuah, L.R. Kneller, Y. Qiu, P.L.W. Tregenna-Piggott, C.M. Brown, J.R.D. Copley, and R.M. Dimeo, DAVE: A comprehensive software suite for the reduction, visualization, and analysis of low energy neutron spectroscopic data, *J. Res. Natl. Inst. Stan. Technol.* **114**, 341 (2009).
- [46] R. A. Ewings, A. Buts, M. D. Le, J. van Duijn, I. Bustinduy, T. G. Perring., HORACE: Software for the analysis of data from single crystal spectroscopy experiments at time-of-flight neutron instruments, *Nucl. Instrum. and Methods in Phys. Res. Sec A*, **834**, 132-142 (2016).
- [47] S. Toth, B. Lake, Linear spin wave theory for single-Q incommensurate magnetic structures. *J. Phys. Condens. Matter* **27**, 166002 (2014).
- [48] R. Yadav, N. A. Bogdanov, V. M. Katukuri, S. Nishimoto, J. van den Brink, L. Hozoi, Spin-orbit excitation energies, anisotropic exchange, and magnetic phases of honeycomb α - RuCl_3 , *Sci. Rep.* **6**, 37925 (2016).
- [49] L. J. Sandilands, Y. Tian, A. A. Reijnders, H-S. Kim, K. W. Plumb, and Y-J. Kim, H-Y. Kee, K. S. Burch, Spin-orbit excitations and electronic structure of the putative Kitaev magnet α - RuCl_3 , *Phys. Rev. B*, **93**, 075114 (2016).
- [50] G.L. Squires, 'Introduction to the Theory of Thermal Neutron Scattering', 3rd edition, University of Cambridge Press (2012).
- [51] J. Chaloupka, G. Khaliullin, Magnetic anisotropy in the Kitaev model systems Na_2IrO_3 and RuCl_3 , *Phys. Rev. B* **94**, 064435 (2016).

- [52] X.-Y. Song, Y.-Z. You, and L. Balents, Low-Energy Spin Dynamics of the Honeycomb Spin Liquid Beyond the Kitaev Limit *Phys. Rev. Lett.* **117**, 037209 (2016).
- [53] B. Lake, A. Tennant, C.D. Frost, S.E. Nagler, Quantum criticality and universal scaling of a quantum antiferromagnet, *Nature Mat.* **4**, 329 - 334 (2005).
-

Acknowledgements:

The authors acknowledge valuable discussions with C. Batista, K. Burch, H. Cao, B. Chakoumakos, G. Jackeli, G. Khalliulin, J. Leiner, P. Kelley, R. Valenti and S. Winter. J. K. and R. M. particularly thank J. Chalker and D. Kovrizhin for collaboration on closely related work. We thank O. Garlea for assistance with the measurement on HYSPEC. The work at ORNL's Spallation Neutron Source was supported by the United States Department of Energy (US-DOE), Office of Science, Basic Energy Sciences (BES), Scientific User Facilities Division. Part of the research was supported by the US-DOE, Office of Science, Basic Energy Sciences, Materials Sciences and Engineering Division (JY and CB). DM was funded in part by the Gordon and Betty Moore Foundation's EPiQS Initiative through Grant GBMF4416. The work at Dresden was in part supported by DFG grant SFB 1143 (JK and RM), and by a fellowship within the Postdoc-Program of the German Academic Exchange Service (DAAD) (JK). The collaboration as a whole was supported by the Helmholtz Virtual Institute "New States of Matter and their Excitations" initiative. The data presented in this manuscript is available from the coauthors upon request.



Supplementary Materials for

Neutron scattering in the proximate quantum spin liquid α -RuCl₃

Arnab Banerjee, Jiaqiang Yan, Johannes Knolle, Craig A. Bridges, Matthew B. Stone,
Mark D. Lumsden, David G. Mandrus, David A. Tennant, Roderich Moessner,
Stephen E. Nagler

Correspondence to: banerjeea@ornl.gov (A.B.); naglerse@ornl.gov (S.E.N.)

This PDF file includes:

Materials and Methods

Supplementary Text

Figs. S1 to S11

Table S1

References

Materials and Methods

Sample preparation and characterization:

Commercial RuCl_3 powder procured from Sigma-Aldrich was purified in-house. The resulting powder is better than 99.9 % pure RuCl_3 , confirmed using Inductive-Coupled Plasma mass spectroscopy (Galbraith Laboratories, Inc.) and X-Ray diffraction using a PANalytical Empyrean X-ray diffractometer, consistent with the earlier results (25). Single crystals of $\alpha\text{-RuCl}_3$ were grown from this purified powder using the vapor-transport technique. All the single-crystal data shown in this manuscript as well as reference (26) were collected on samples from the same growth batch. The temperature dependence of the magnetic susceptibility (Fig. S1) was obtained using a Quantum Design magnetic property measurement system (MPMS) in the temperature range of 2 K-320 K. This shows just one magnetic transition at $T_N = 7$ K (see Fig S1B inset) consistent with reference (26). The main panel of Fig. S1B shows the inverse susceptibility ($1/\chi$) measured with field in and out-of-plane. A linear fit in the high-temperature limit ($T = 170 - 320$ K) shows that these have similar slopes corresponding to an effective high-temperature moment of roughly $\mu = 2.35 \mu_B$. Below ~ 120 K (shown by black arrow) the in-plane inverse susceptibility deviates from linearity, however the out-of-plane susceptibility does not show this behavior. The extrapolated Curie-Weiss temperatures (Fig. S1 caption) are overall close to recently published literature on bulk measurement in single-crystal $\alpha\text{-RuCl}_3$ (35, 36). The temperature dependence of the resistivity is shown in Fig. S1B, showing a room temperature Arrhenius gap of 0.4 eV. This is consistent with the recent consensus that $\alpha\text{-RuCl}_3$ is a Mott insulator (21, 37, 38).

The magnetic structure of the large crystal used in this study is the same as that found in the structural study reported in Ref (26), with a zigzag structure in each plane stacked with a 3-fold periodicity. This is illustrated by an elastic cut in the scattering along $(1/2, 0 L)$ (trigonal notation) as seen in Fig. S1C, showing peak positions at $L = n$ (integer) with a systematic absence of the $L = 3n$ peaks. For simplicity of representation the manuscript uses trigonal wave vector with lattice parameters consistent with (25).

Neutron diffraction and 4D inelastic neutron scattering (INS):

All neutron scattering was performed on one single piece of crystal about 490 mg in mass and $1.5 \times 4.0 \times 0.1 \text{ cm}^3$ in size. This was sealed in a thin walled aluminum canister with 1 atmosphere Helium gas in order to both avoid moisture and provide a thermal anchor. The low T crystal structure of the sample is consistent with previous reports (22, 26, 41). Neutron scattering measurements were carried out using the SEQUOIA chopper spectrometer (42, 43) at the Spallation Neutron Source (SNS), except for the data shown in Figure 1B which was measured using the HYSPEC (42) instrument ($E_i = 15 \text{ meV}$, Fermi chopper spinning at 360 Hz). Elastic neutron scattering at both instruments showed the low temperature magnetic order is consistent with reference (26): an in-plane zigzag structure with a 3 layer stacking periodicity (see Fig S1C). The sample showed a single magnetic transition at 7 K and no evidence for ABAB type stacking contamination (i.e., no $(1/2 \ 0 \ 3/2)$ (trigonal notation) order peaks). The ratios of magnetic and nuclear

Bragg peak intensities measured here are consistent within measurement uncertainty with those reported in reference (26).

For INS measurements reported here the sample was sealed in a thin-walled can with He contact gas and mounted in a closed-cycle Helium based refrigerator for temperature control. Most measurements used an incident energy of $E_i = 40$ meV ($\lambda = 1.43$ Å) was used with the T_0 chopper at 60 Hz and Fermi chopper at 360 Hz (42). The resolution of the instrument with this setting is 1.10 meV FWHM (full width at half maximum) at the elastic position and 0.96 FWHM meV at 6 meV energy transfer. The 2D detectors at SEQUOIA covered an angular range of up to 54° in the horizontal plane and $\pm 18^\circ$ in the vertical plane corresponding to an overall solid angle of 0.863 steradians (43). For ease of discussion and consistency with the 2D honeycomb lattice the Q dependence of the inelastic scattering in this paper is plotted using the notation of the trigonal space-group ($P3_112$, $a=b=5.975$ Å, $c=17$ Å, $\alpha=\beta=90^\circ$, $\gamma=120^\circ$). In this notation, the reduced data is plotted along the orthogonal axes (1,1,0), (1,-1,0) and (0,0,1), denoted in this paper by (H,H,0), (K,-K,0) and (0,0,L). The (H,H,0) axis is in units of 2.10 Å⁻¹, the (K,-K,0) axis is in units of 1.21 Å⁻¹, and the (0,0,L) axis is in units of 0.37 Å⁻¹. The corresponding coordinates in the orthogonal $C2/m$ space group symmetry (22, 26) would be (2,0,0), (0,2,0) and (0,0,1/3), respectively. See Section B for a discussion on BZ.

For INS, the crystal was mounted with the (H,H,0) and (0,0,L) axes in the horizontal plane, and the orthogonal (K,-K,0) axis pointing vertically upwards. A tomographic reconstruction in momentum space was performed by rotating the crystal about the (K,-K,0) axis over 360° (in 2.5° steps for 5 K data, and 5° steps for 10 K and 120 K data), measuring for a fixed amount of proton charge on the spallation target (roughly 15 minutes per measurement). This provides a continuous coverage over all the three orthogonal momentum-transfer dimensions (H,H,0), (K,-K,0) and (0,0,L). The 4th dimension of energy-transfer was obtained via the time-of-flight of the neutrons. The individual measurements at each rotation angle were normalized for the proton charge on the spallation target, corrected for detector sensitivity using vanadium normalization, and then binned from 4D laboratory coordinates to 4D sample coordinates using standard direct geometry chopper spectrometer reduction routines within the Mantid software (44) with an energy bin of 0.4 meV and momentum bin of 0.04 Å⁻¹. Data from both the sample and the empty canister background were reduced in an identical fashion as above.

Data analysis:

The data was subtracted of the background, rebinned, and projections along the appropriate crystallographic axes were made for presentation and analysis purposes using MSlice distributed by the DAVE project (45) and HORACE software distributed by ISIS (46). The plots were made using Matlab. The spin wave calculation in fig 3e was performed in Matlab using SpinW package (47). The neutron intensities derived for the Kitaev model started from the exact dynamical structure factor calculated as described in references (12) and (13) and accounted for neutron polarization terms and the spherically approximated magnetic form factor of Ru³⁺ in the same manner as described in reference (25). Additional details presented below in the Supplementary Materials Section C on ‘Neutron scattering cross section on pure Kitaev model’.

Supplementary Text

A. Single-ion states in α -RuCl₃ and Kitaev interactions

It has been shown (15) that Kitaev terms can arise in the effective spin Hamiltonian for transition metal ions under the following conditions: (i) The ions have a d^5 configuration in a strong octahedral crystal field leading to the low spin state. (ii) Spin-orbit coupling (SOC) is sufficient to ensure a $J_{eff} = 1/2$ single-ion ground state over the relevant temperature range. (iii) The octahedra are edge sharing. As has been discussed widely in the literature, the Ru³⁺ ions in α -RuCl₃ are centered in edge-sharing octahedra of Cl⁻ ions in the low spin state, with SOC leading to an effective $J_{eff} = 1/2$ ground state (21, 25, 38-40, 48, 49). The $J_{eff} = 1/2$ to $J_{eff} = 3/2$ splitting in α -RuCl₃ has been measured directly using neutron scattering as 195(11) meV (25), corresponding to thermal energy scales of more than 2000 K. See Figure 2 of reference (25) for the data as well as an energy level scheme.

B. Real and reciprocal space definitions

Although at low temperatures the crystals have been identified as showing a monoclinic $C2/m$ space group (22, 26), the honeycomb lattice of Ru³⁺ atoms in each plane is symmetric to <0.2 % (26). Moreover, there are three possible monoclinic domains related by 120° rotations. The in-plane dependence of the inelastic scattering is best depicted using the reciprocal space appropriate for the honeycomb lattice, which is the same as the in-plane reciprocal lattice of the trigonal space group structure. All calculations for the pure Kitaev model and the data can be similarly reproduced using a $C2/m$ type space group, and the conclusions presented in this paper hold regardless. In Fig S2A, we show the in-plane real space lattice vectors for trigonal and monoclinic structures; the honeycomb reciprocal space is shown in Fig. S2B. For ease of comparison, the reciprocal space diagram is plotted over the same range as in Fig. 4, A and B.

Figure S3 shows the elastic scattering data ($E = [-0.25, 0.25]$ meV) taken with $E_i = 25$ meV, at $T = 5$ K $< T_N$. This shows the magnetic Bragg peaks in the HK plane, plotted over the same range as in fig. 2 of main text. The reciprocal space Brillouin Zone (BZ) diagram is superimposed to give a perspective on the extent of the data. The reciprocal lattice vectors are marked by red arrows. Magnetic Bragg peaks (faint green or red dots) appear at the M points ((1/2,0,L) type points), while the structural Bragg peaks (intense red dots) appear at the (1,0,L) type points.

C. The neutron scattering cross section calculations for the pure Kitaev model

The neutron scattering cross section calculations for the pure Kitaev model needed to compare to the experimental data are obtained by utilizing the known exact calculations of the zero-temperature dynamic response functions (12, 13), and subsequently accounting for the neutron polarization factors and the Ru³⁺ form factor (25).

We outline some aspects of the exact calculation for the isotropic Kitaev model below, for details see (12, 13). In the Kitaev model spins fractionalize into static Z_2 gauge fluxes and itinerant Majorana fermions. The dynamic magnetic response function can be expressed as a Fourier transform of the spin-spin correlation function (following equation 2 in (12), adopting a Pauli Matrix notation):

$$S^{aa}(\vec{q}, \omega) = \frac{1}{N} \sum_{ij} \exp(-i\vec{q} \cdot \mathbf{r}_{ij}^a) \int_{-\infty}^{\infty} \langle \hat{\sigma}_i^a(0) \hat{\sigma}_j^a(t) \rangle \exp(i\omega t) dt \quad \dots \text{(SE1)}$$

Here \mathbf{r}_{ij}^a is the vector connecting spin-1/2 degrees of freedom between nearest neighbor (NN) sites i and j for the bond type $a=\alpha, \beta$ or γ of the honeycomb lattice as explained in Fig. 1a of the main text. The calculation of the correlation function is facilitated by the fact that fluxes are non-dynamical -- the action of a spin operator inserts a static nearest-neighbor (NN) flux pair. For a nonzero matrix element the second spin operator acting at a later time needs to remove the same fluxes, leading to ultra-short ranged correlations in real space, e.g. $S_{ij}=0$ for $\langle i, j \rangle$ any further than NN apart (11). For the remaining onsite correlators $S_0 = S_{ii}^{aa}(\omega)$ and NN correlators $S_1 = S_{ij}^{aa}(\omega)$ (independent of aa for isotropic couplings) it is possible to obtain an expression in terms of Majorana fermions (12). This takes the form of a local quantum quench of Majoranas which can be solved numerically exactly even in the thermodynamic limit (12, 13). The resulting functions S_0 and S_1 are continuous functions of energy. While the onsite correlation S_0 is always positive as a function of frequency the NN component S_1 changes sign above $\omega \sim 0.8 K$ as shown in figure S4. Substituting these results into equation SE1 yields:

$$S^{aa}(\vec{q}, \omega) = 2(S_0(\omega) - \text{sgn}(K) \cos(\vec{q} \cdot \vec{R}_{NN}^a) \cdot S_1(\omega)) \quad \dots \text{(SE2)}$$

Here the nearest neighbor correlator is given by each type of honeycomb bond $\vec{R}_{NN}^a = \vec{r}_i - \vec{r}_j$. The term $\text{sgn}(K) = +1$ for AFM Kitaev interactions and -1 for FM Kitaev interactions (12, 13). Eq. SE2 implies that over the broad region near $E \approx K$ where S_1 is negative the AF response has a peak at the Γ point, while the FM response has a local minimum. (Note: We are setting $\hbar = 1$ so that E and ω are used interchangeably here).

To make contact with the experimental neutron scattering cross-section one needs to take into account the neutron polarization factors, relevant anisotropies and the magnetic form factor $F(q)$ (50). This leads to an expression for the scattering intensity:

$$I(\vec{q}, \omega) \propto |F(q)|^2 \sum_{a=\alpha, \beta, \gamma} (g_{aa})^2 \left\{ S^{aa}(\vec{q}, \omega) \left(1 - \left(\frac{q^a}{q} \right)^2 \right) \right\} \quad \dots \text{(SE3)}$$

where q^a is the projection of the momentum vector on the direction of the spin components, the explicit inclusion of g_{aa} accounts for anisotropy in the g -tensor, and $F(q)$ is the magnetic form factor. For the purposes of this calculation we have made the simplifying assumption that the Ru^{3+} form factor is isotropic. This assumption is well justified for small q near the Γ point, although for measurements of the magnetic scattering beyond the 2nd Brillouin zone anisotropy of the form factor may become important.

The mechanics of the calculation utilizes spin axes where the $\langle 111 \rangle$ direction in spin space is perpendicular to the honeycomb plane, and the projections of the $\langle 100 \rangle$, $\langle 010 \rangle$, and $\langle 001 \rangle$ directions are naturally separated by 120° in the plane (16). We note that the primary anisotropy in the g -factors is between the in-plane and out of plane directions. Therefore, if anisotropy within the honeycomb plane is ignored, isotropic g factors can be employed in the calculation. The relatively small in-plane anisotropy will be further averaged out by domains. In the discussion below we use an isotropic g factor for simplicity.

The result of SE3 plotted in the ab -plane is shown for AFM Kitaev interactions in Fig. S5B and for FM Kitaev interactions in Fig. S5C. For a visual reference, Fig 4A from the main text is also presented at the top.

The exact solution of the Kitaev model captures the qualitative features of the data, e.g., the symmetry and periodicity in the BZ and, most importantly, a maximum of intensity around the Γ point extending over a large fraction of the BZ and a very broad energy range. For the AF Kitaev model, as a function of energy, a local intensity maximum close to the Γ point occurs near $E = 1.2$ K, which is similar to the location of the maximum in the powder-averaged model (25). When comparing to experiment there are quantitative differences from the Kitaev model expected to arise from the additional interactions which are also responsible for the low temperature magnetic long range order. As a first step to account for this empirically, keeping the assumption of short-ranged NN spin correlations only, we introduce a single multiplicative fitting parameter, C_l on the NN correlator S_l ,

$$I(\vec{q}, \omega, C_l) \propto |gF(q)|^2 \times \sum_{\alpha=\alpha,\beta,\gamma} \left\{ \left(S_0(\omega) - C_l \text{sgn}(K) \cos(\vec{q} \cdot \vec{R}_{NN}^{\alpha}) \right) \cdot S_l(\omega) \left(1 - \left(\frac{q^{\alpha}}{q} \right)^2 \right) \right\} \dots \text{(SE4)}$$

This equation is fit to the data of the cut shown in Fig. 4C in the main text, for $E = 1.2$ K we obtain $C_l = 2.0 \pm 0.1$. In fact the fitted value of C_l is not very sensitive to the value of E/K over the range $1 \leq E/K \leq 1.4$. This indicates that the ratio of the NN to onsite correlator in α -RuCl₃ is enhanced by a factor of roughly 2 (Note, this is same as the factor ‘ R ’ in the main text).

We note that one expects the low frequency dynamics of the material to be strongly affected by smaller non-Kitaev terms in the Hamiltonian, and it is not appropriate to compare data in that regime to the calculation above*. In the ordered states one observes spin waves that are seen to disappear at temperatures just above T_N . Nevertheless it is interesting to consider whether spin waves can explain a continuum response at the Γ point. We have calculated spin waves for many different model Hamiltonians with K, J_l, J_2, Γ , (some of which are described in Supplementary Information of (25)). Although many allow for some response at the fixed energies at the Γ point, we have not found any that yield the correct scattering over a broad energy continuum. As an example, the DFT (31, 32) and quantum chemistry calculations (48, 51) performed by various groups using

inputs from structure and susceptibility measurements (22, 26, 33) and references therein, predict a FM Kitaev term $K \sim -J$. A plot of the classical spin wave dispersion relation for a representative set of parameters ($K=-J=-6$ meV, $J_I=-0.75$ meV, $J_3 = 0.0^+$, summed over the three 120° domains (26)) in that regime is presented in Fig. S6A-C. Although at lower energies it seems to be roughly consistent with the data at the M points, the in-plane intensity distribution for higher energies (for e.g. $E > 3$ meV) has no intensity at the Γ -point. At any rate, our data shows that the scattering at the Γ point extends to 10-15 meV and is strongly present even at $T = 120$ K, much higher than T_N (and hence beyond the purview of any spin wave calculation), as shown in Fig. S6D.

*A recent study of the role of small perturbations from the Kitaev point (52) shows how the response function is modified particularly at low energies, i.e. below the flux gap. The relevant energy window is not accessible in the current experiment.

D. Comparison of constant Q cuts to the scattering from the AF Kitaev model with $R=2$

The scattering cuts plotted near the 2D Γ point (see Figs. 3A and B, and Fig. 6D) are integrated over a range of reciprocal space chosen to give adequate statistics such that the precision in the intensity at 10 meV is $\Delta I/I \approx 10\%$. Figure S7 shows cuts at three wavevectors at a temperature of $T = 10$ K integrated over much narrower ranges of reciprocal space. With such narrow integration ranges it is challenging to attain statistics sufficient to make a reasonable comparison with theoretical models, so in addition, the data have been assumed symmetric and symmetrized where possible to enhance the statistics. These are compared to a calculation of the neutron cross-section for a $T=0$ antiferromagnetic Kitaev model with a value $K = 5.5$ meV (extracted in reference (25)) and $C_I = R = 2$. The model uses one uniform scale parameter on the theory and assumes a flat background.

One plot (Fig. S7A) illustrates the model with the flat background allowed to vary with Q, and the other plot (Fig. S7B) shows the result assuming that the background is kept the same at all values of Q. The first plot (Fig. S7A) shows that the AF Kitaev model using the same Kitaev energy extracted in Ref. (25) gives a qualitatively reasonable description of the width of the high energy side of the continuum and of the relative intensity as a function of Q. A comparison is also shown to the scattering from a collection of non-interacting Ising dimers. The dimer scattering, which is broadened by the energy resolution of the spectrometer, is seen to be very narrow in energy compared to the data, and also shows an intensity fall off with increasing Q that is much slower than seen experimentally. The second plot (Fig. S7B) shows that the pure Kitaev model describes the data better than a model of Ising dimers even with the highly restrictive assumption of an absolutely constant background of the same value as used in Table S1.

A more complete description of the inelastic scattering in α - RuCl_3 will require a rigorous quantum theory of the as yet undetermined full Hamiltonian. Additional experimental measurements with better statistics and higher resolution will also be beneficial.

E. Extending the pure Kitaev solution by adding an adhoc next-nearest neighbor (NNN) correlation

While many aspects of the high-energy mode are captured by the pure Kitaev model, it does not reproduce the detailed in-plane Q dependence, specifically the six-pointed star-shaped intensity at the Γ -point (Fig 4A). Beyond the possibility that NN correlations are enhanced by non-Kitaev terms, generically non-vanishing longer-range correlators will also be induced. Therefore, here we consider the addition of an adhoc NNN correlator added as a simple fraction C_2 of the NN correlator:

$$I_{NNN}(\vec{q}, \omega, C_1, C_2) \propto C_2 \sum_b \left(\cos(\vec{q} \cdot d_{NNN}^b) \cdot C_1 S_1(\omega) \right) \left(1 - \left(\frac{\vec{q} \cdot d_{NNN}^b}{\bar{q}} \right)^2 \right) \quad \dots \text{(SE5)}$$

Here b sums over the 6 NNN terms for a given Ru^{3+} atom shown in fig. S2B. The final intensity is then SE6 added to:

$$I(q, \omega, C_1, C_2) \propto I(\vec{q}, \omega, C_1) + I_{NNN}(\vec{q}, \omega, C_1, C_2) \quad \dots \text{(SE6)}$$

In Fig. S8 we show the result for $C_2 = -0.1$ (maintaining the S_l multiplier $C_l = 2$), where the NNN correlator is 10 % of the NN correlator but with an opposite sign, which successfully reproduces the star-like shape in the first BZ. This simplistic treatment fails to satisfactorily capture the scattering beyond just the first BZ. It nevertheless shows that correlations that are somewhat extended in real space (compared to the ultra-short ranged Kitaev QSL) account naturally and simply for the star shape.

F. A mean field extension of the pure Kitaev solution

In order to account for the tendency of the material to order at low temperatures, we use a phenomenological mean-field model that allows for a calculation of the response function within the framework of the Random Phase Approximation (RPA). Following earlier work on coupled chains (32), and knowing empirically that $\alpha\text{-RuCl}_3$ forms a zigzag ordered state at low temperatures, we introduce an effective symmetry-breaking zigzag field J_h within a RPA. This modifies the magnetic susceptibility such that

$$\chi_{RPA}(q, \omega) = \frac{\chi(q, \omega)}{1 - 2c_h J_h(q) \chi(q, \omega)} \quad \dots \text{(SE7)}$$

where c_h is a prefactor capturing the strength of J_h .

The RPA calculations start from the complex susceptibility χ , where $Im(\chi)$ is directly proportional to the spin structure factor $S^{aa}(\vec{q}, \omega)$ and $Re(\chi)$ is obtained using the Kramer-Kronig relations. To incorporate the short-range correlations of the zigzag order into J_h we work with the simplest motif of the honeycomb lattice consisting of just three NN bonds as shown in Fig. S9 – the ‘‘Y’’ motif containing four spins. For the zigzag ground state three of these spins will have the same sign and one at the corner will have an opposite sign. The zigzag field at the central atom of the motif is then given by:

$$J_h(q) = \sum_{k=4 \text{ atoms}} (\sigma_k e^{iqd_k}) \quad \dots \text{ (SE8)}$$

where σ_k takes a value of +1 for an up-spin and -1 for down-spin.

We do not want to explicitly break translational or spin-rotational invariance because we are only concerned with data above T_N . Therefore we symmetrize all possible zigzag configurations leading to the averaging of the 12 diagrams shown in Fig. S8. The final result is shown in Fig. S10A and B. For $c_h > 0.2$ the original AF Kitaev intensity (i.e., maintaining $C_I=1$) starts to get visibly modified, with a result of $c_h = 0.35$ qualitatively reproducing best the observed star-like pattern at every 2nd BZ center. Comparing the result to the data in Fig. 4a, we conclude that the RPA calculations go in the right direction to capture some aspects of the Q-dependence of the data beyond the pure Kitaev model, in particular the more pronounced star-like structure in the BZ. We note that a full RPA calculation would start from a model Hamiltonian and properly treat the small terms of the pure Kitaev calculation in a perturbative fashion, however the present mean field approximation gives a general idea of the results that one should expect.

G. High frequency vs. low frequency dynamics

Evaluations of various spin-wave theory (SWT) descriptions for α -RuCl₃ have been considered previously (25). In principle SWT can give a good description of the low energy excitations in a system with long range order even when the high energy spectrum is dominated by quantum fluctuations. A classic example is provided by coupled S=1/2 antiferromagnetic Heisenberg chains, with experiments exemplified by KCuF₃ (see, for e.g., Ref (53)). The situation in α -RuCl₃ is believed to be similar, in the sense that spin wave excitations are present at low energies below T_N while the fractionalized excitation continuum persists at high energies for T above and below T_N .

Most estimates of the low-energy effective Hamiltonian for α -RuCl₃ using DFT find the Kitaev interaction to be ferromagnetic, with a substantial contribution from off diagonal exchange and Heisenberg exchange to at least third neighbor spins (31, 33, 34, 51). The starting point for the DFT is a perfectly ordered static structure, and the derived low-energy effective Hamiltonian depends sensitively on the precise values of bond angles and distances in the structure. In the actual material there can be disorder due to defects such as stacking faults; moreover there are substantial low frequency vibrational excitations including some that are quasi-2D. These deviations, from a structure that is both static and regular, raise the possibility of a modified effective Hamiltonian describing the actual physics seen by the neutrons, in particular at higher frequencies. The nature and size of such effects, including perhaps even on the sign of the Kitaev interaction, will need to be evaluated in the future (31, 34, 48, 51).

H. A note on the orientationally-averaged spectra of current data

Single crystal data has a significant advantage over powder data as it allows measurements at specific points in reciprocal space, enabling a differentiation between different points in the two-dimensional Brillouin zone, for example, Γ and M points. Powder averaging the data mixes all wave-vectors with the same magnitude. Nevertheless it can be instructive to compare pseudo-powder averaged single crystal data with measurements on true powders.

Figure S11 shows orientationally averaged data from the single crystal and a comparison with the powder data of Ref (25). Notwithstanding that the measuring conditions were not the same, above T_N the spectra look nearly identical. Below T_N , the data in the region of the “upper mode” near 6.5 meV shows no change in either sample. However, at low energies, the data differ, reflecting the fact that the single crystal used here and the powder used in Ref. (25) order at different temperatures with different wave-vectors.

We note that a “powder averaged” single-crystal data is necessarily different from true powder measurements (25) in the following respects:

1. An actual powder experiment provides a measurement of a weighted density of states averaged over all possible orientations of the system. The data from the single crystal is averaged only over the orientations of the crystal where data exists, as opposed to the full set of orientations. In the course of the single crystal measurement the sample was rotated only about one axis. Therefore the sampling of the density of states is less complete than it is in an actual powder.
2. The powder sample measured in reference (25) was a 5 gram sample; the single crystal is slightly less than 1/10 of this mass, and the statistics in the orientationally-averaged single crystal data reflects that fact. Notably, background features that are small compared to the signal in a restricted region of reciprocal space in a single crystal can become very significant when the signal is averaged over all orientations.
3. The single crystal data was measured with a higher incident neutron energy than the powder data ($E_i = 40$ meV vs. $E_i = 25$ meV) and therefore, the energy resolution in the single crystal data is lower.
4. The powders order at $T_N = 14$ K, with the zig-zag layers antiferromagnetically coupled (25). Our pristine single crystals order at $T_N = 7$ K with honeycomb zig-zag layers stacked with a three-fold periodicity (26) (also see Fig S1C). The details of the spin-wave spectrum associated with the ordered magnetic ground state will not be identical between these two cases. However this does not affect the response at intermediate energies.

Figures S11 A/B show pseudo-powder averaged single crystal data at temperatures below/above T_N . These figures can be compared with the true powder measurements in reference (25) Fig. 3a. Given the caveats mentioned above, the essential conclusions from both the data sets are consistent. Below T_N there are two peaks in the density of states. The broad upper energy feature occurs close to $E = 6.5$ meV in both samples, and in contrast to the lower energy feature, is essentially unaffected by the transition at T_N .

Figures S11C/D show the corresponding constant-Q cuts integrated in the interval $Q = [0.5, 1.25] \text{ \AA}^{-1}$ with intensity plotted as a function of energy. The “upper mode” around 6.5 meV is similar in both the single crystal and powder samples both above and below T_N . Below T_N it is apparent that the low energy spectra are different. This part of the spectrum reflects spin wave excitations from the magnetically ordered system. Within each honeycomb layer the magnetic moments order in a zigzag pattern. However, the true powder orders at $T_N = 14$ K, with ordering wave-vectors reflecting a two layer magnetic repeat pattern, while the single crystals order at $T_N = 7$ K with a three layer repeat pattern. It is therefore quite likely that the spin wave density of states differs in the two systems and in that case one would expect the average energy to be higher in the powder since it has a higher T_N . As seen in Fig. S10C the magnetic density of states in the powder is peaked near 4 meV, while in the single crystal it is near 3 meV. One cannot completely preclude the possibility that a difference also arises as an artifact of different sampling of Brillouin zones for single crystal and powder. Moreover, it is possible that the underlying crystal structures of the single crystal and powder samples reflect different polytypes. Sorting out all of these details in α -RuCl₃ will require additional research.

Supplementary Figures

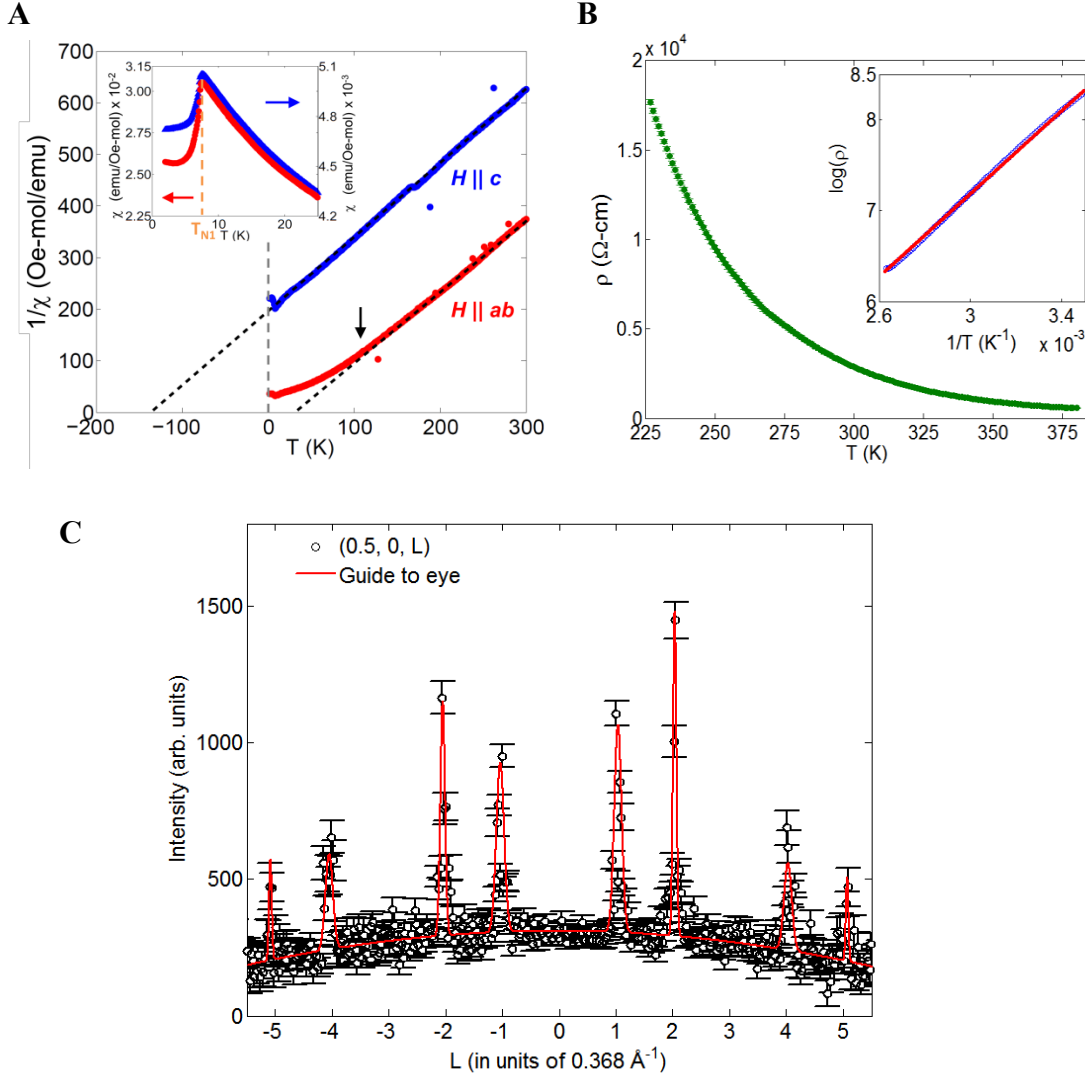


Fig. S1.

(A) The Inverse susceptibility of pure α - RuCl_3 measured with $H||ab$ (red) and $H||c$ (blue) is fitted to a linear behavior in the regime 150 K – 300 K to yield an effective moment size of $\mu=2.39(2) \mu_B$ and $\mu=2.33(2) \mu_B$ for in-plane and out-of-plane measurements respectively with the extrapolated Curie-Weiss temperatures are $\theta_c = -130(4)$ K for $\chi||c$ and $\theta_{ab} = 32(3)$ K for $\chi||ab$. (B) The resistivity of a single-crystal of α - RuCl_3 from the same batch as the crystal in Fig 1 shows an activated (Arrhenius) behavior $\rho=\rho_0 \exp(\Delta/2kT)$ corresponding to an insulating gap of $\Delta\sim 400$ meV at room-temperature (inset). (C) Cut on the SEQUOIA $E_i = 40$ meV data at $T = 5$ K on the elastic plane along $(1/2, 0, L)$ integrated in the range $\Delta E=[-0.25, 0.25]$ meV, $\Delta H=[-0.1, 0.1]$, $\Delta K=[0.45, 0.55]$. This shows magnetic Bragg peaks with the selection rules (e.g., missing $(1/2, 0, L)$ for $L=3n, n=\text{integer}$) consistent the structure reported in Ref. (26).

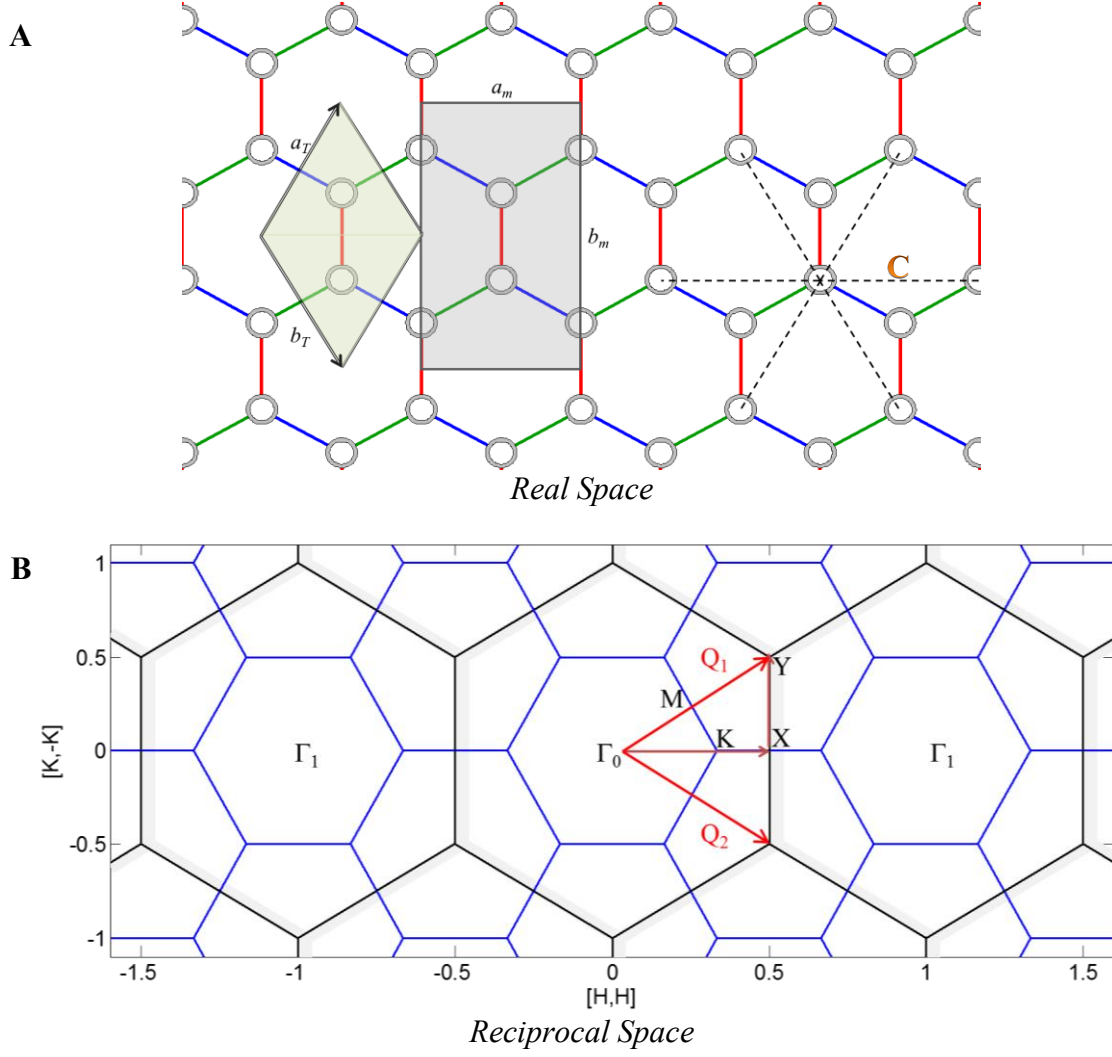


Fig. S2. (A) The honeycomb lattice showing the locations of the Ru^{3+} (empty circles). The unit cells for the trigonal and monoclinic space groups are shaded. a_T and b_T are the lattice vectors in a trigonal space group as used in this paper, while a_m and b_m are the the corresponding lattice vectors for the monoclinic space group (22, 26, 34). The black dashed lines show the 6 next nearest neighbors for the atom in the center marked ‘C’. (B) The reciprocal lattice of the honeycomb lattice in the trigonal space group. \vec{Q}_1 and \vec{Q}_2 (red arrows) are the reciprocal lattice unit-vectors for the unit-cell parameters a_T and b_T in fig. S2A. The blue and black hexagons are the 1st and 2nd BZ respectively in the trigonal description. The corresponding reciprocal high-symmetry points are marked.

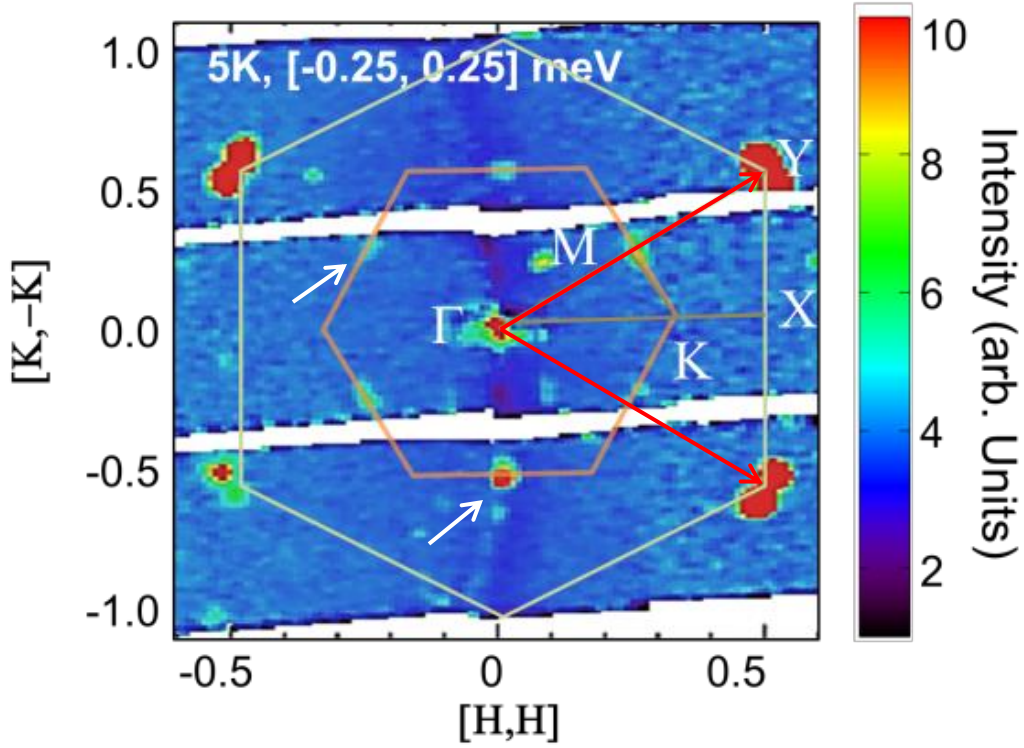


Fig. S3.

The same reciprocal space image as in Fig. S2B when superimposed on top of the data taken at SEQUOIA with $E_i = 25$ meV, $T = 5$ K, integrated at the elastic location $E = [-0.25, 0.25]$ meV and $L = [-2, 2]$. The smaller orange hexagon and the larger grey hexagon represent the 1st and the 2nd Brillouin Zones respectively. The red arrows mark the two reciprocal lattice vectors \vec{Q}_1 and \vec{Q}_2 similar to Fig S2B. The magnetic Bragg peaks are apparent as green/red dots at the M points (centers of the sides of the orange hexagon, examples indicated by white arrows). The white regions lack detector coverage.

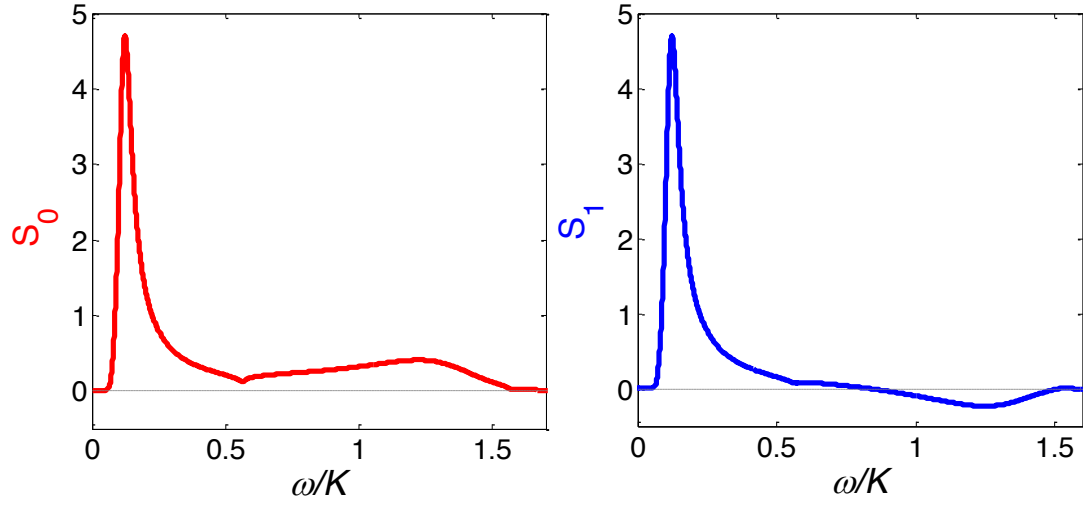


Fig. S4.
The functions S_0 and S_1 plotted versus ω (in units of the Kitaev energy K).

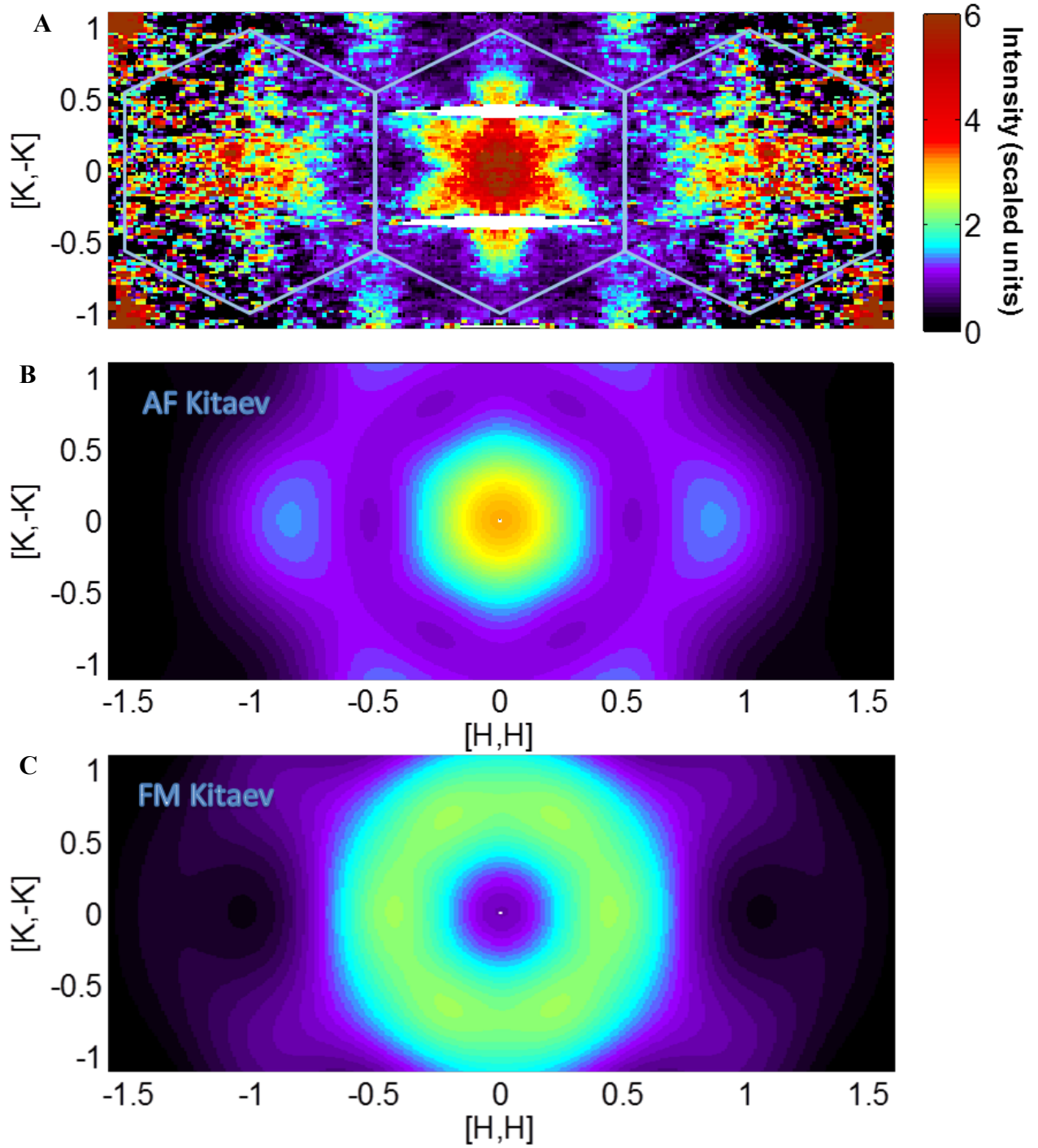


Fig. S5.

(A) The data from Fig 4a of main text. The 2nd BZ is superimposed (light blue lines)
 (B&C): The intensity distribution of the pure Kitaev calculation with $E = 1.2$ K for the AF Kitaev model (B) and the FM Kitaev model (C) including the neutron polarization factor and the spherically approximated Ru^{3+} form factor.

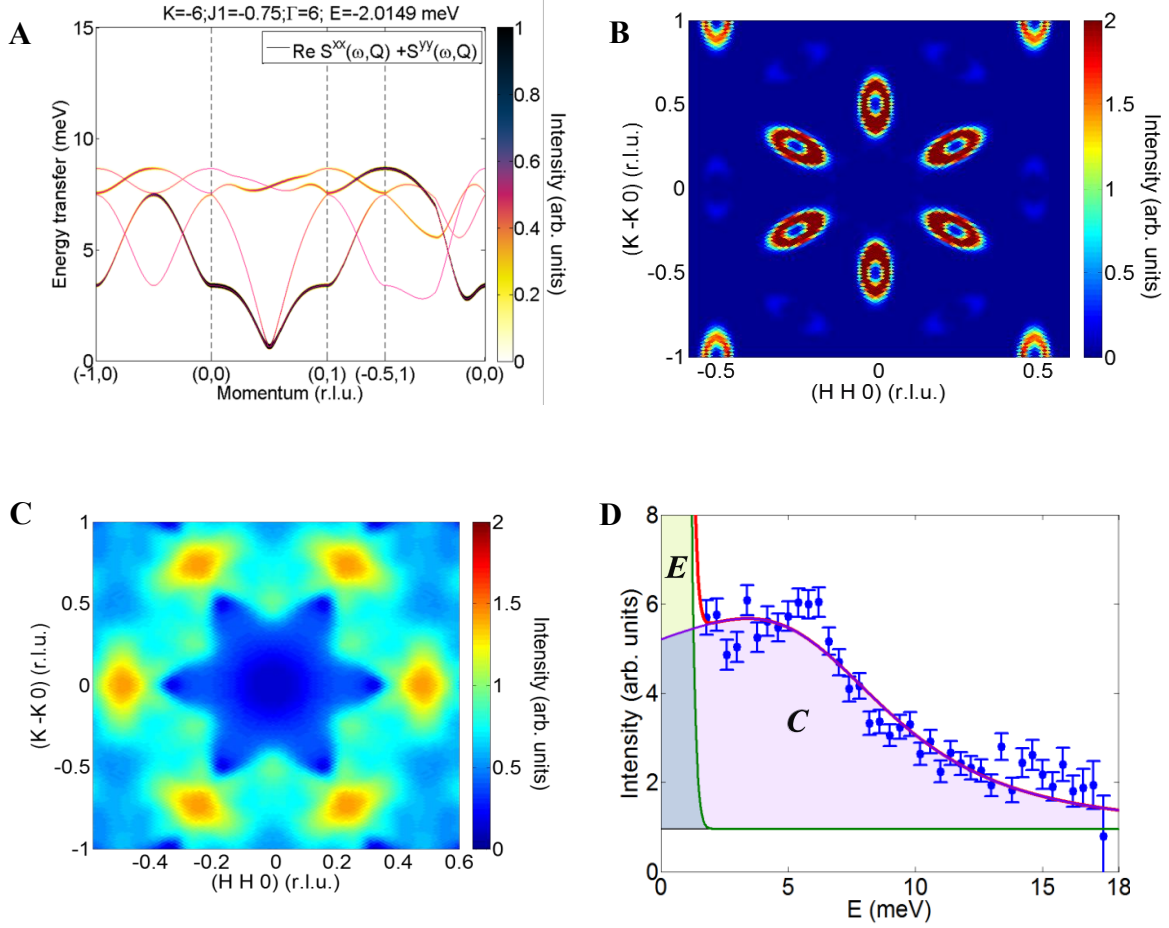


Fig. S6.

(A) The SWT dispersions of a FM Kitaev model with parameters $K=-\Gamma=-6$ meV and $J_I=-0.75$ meV. (B) Calculated SWT intensity slice at $E = [1.5, 2.0]$. (C) The constant energy slice at a higher energy $E = [6, 10]$ meV lacks significant intensity at the Γ point. (D) The cut through the $E_i = 40$ meV, $T=120$ K data shows that the scattering at the Γ -point is persistent up to a temperature several times T_N . ‘E’ is the scattering from the elastic line and ‘C’ is the continuum as defined for Fig 3(A)(B). The elastic contribution at $E = 0$ is fit to a Gaussian function with width equal to the instrument resolution, and the continuum ‘C’ is fit to a DHO (See Table S1 for the relevant fit parameters).

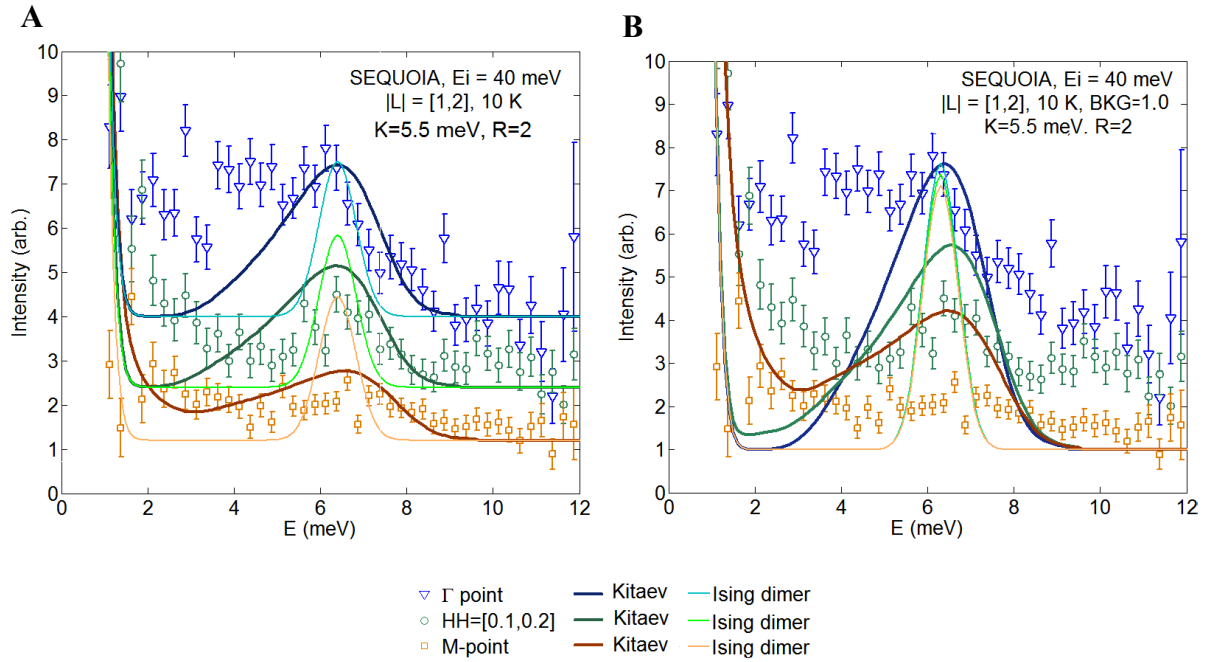


Fig. S7.

The $E_i = 40$ meV SEQUOIA data at $T = 10$ K is cut over narrow reciprocal-space volumes to show the wave vector dependence of the intensity profiles below 12 meV. For increased statistics, the data is symmetrized along the $\xi = 0$, $\zeta = 0$ and $L = 0$, where ξ and ζ are (H,H) and (K,-K) respectively, defined as in the caption of figure 3 of main text. Each cut represents an integrated Q-space volume $\Delta\xi\sqrt{3} = \Delta\zeta = 0.1$; $\Delta L = 1$. Data at three Q-points are shown: the Γ -point ($[\xi, \zeta] = [0, 0]$, blue triangles), between Γ and K points ($[\xi, \zeta] = [0.15, 0]$, green circles), and at the M-point ($[\xi, \zeta] = [0, 0.5]$, brown squares). The corresponding scattering from a pure zero-temperature Kitaev model is calculated at the same above locations with $K = 5.5$ meV (25) and $C_I = R = 2$, using a uniform scale factor (see section C for details). The scale factor is chosen so that the calculated scattering for the Γ point matches the height of the data at ~ 6 meV. The calculations also include an elastic peak and a flat background. For comparison we also plot the scattering expected from a system of superposition of Ising dimers directed along the Ru-Ru bonds, using the same flat background. The dimer response is a delta function in energy but is broadened by the instrumental resolution. (See key for color codes). (A) The flat background is allowed to vary as a function of Q; the appropriate background is seen to be somewhat higher at smaller Q. (B) The flat background is artificially restricted at the same value used in Table S1.

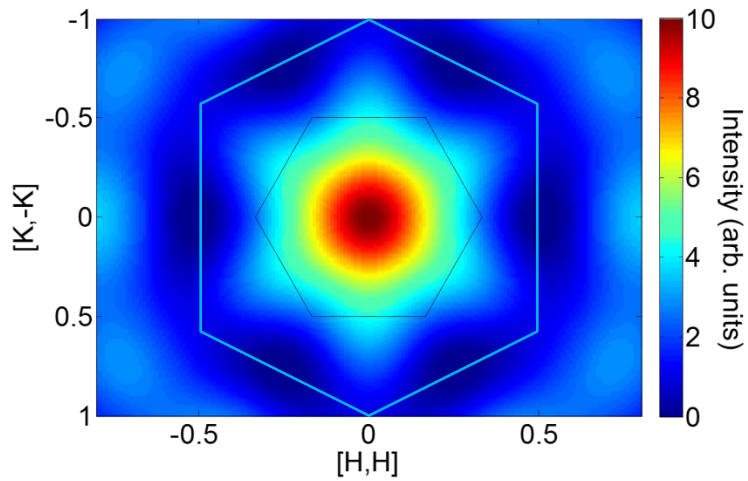


Fig. S8.

The pure Kitaev calculation with a next-nearest neighbor correlator as described in text, resembles a star pattern at the Γ -point.

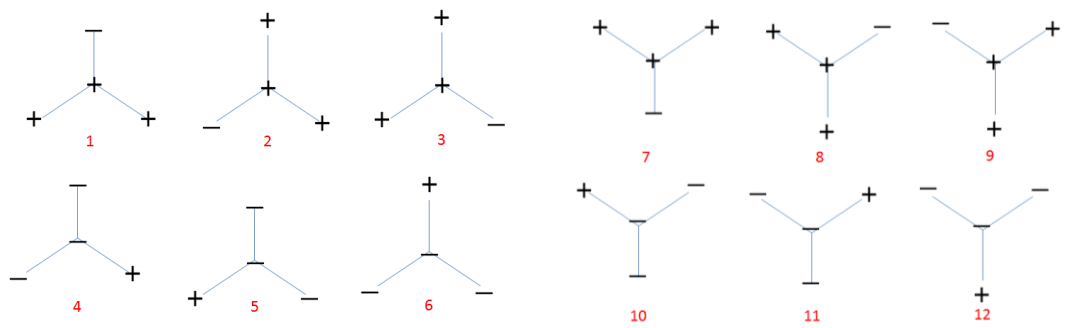


Fig. S9.

The 12 possibilities summed up for RPA to preserve symmetry. Details in supplementary text.

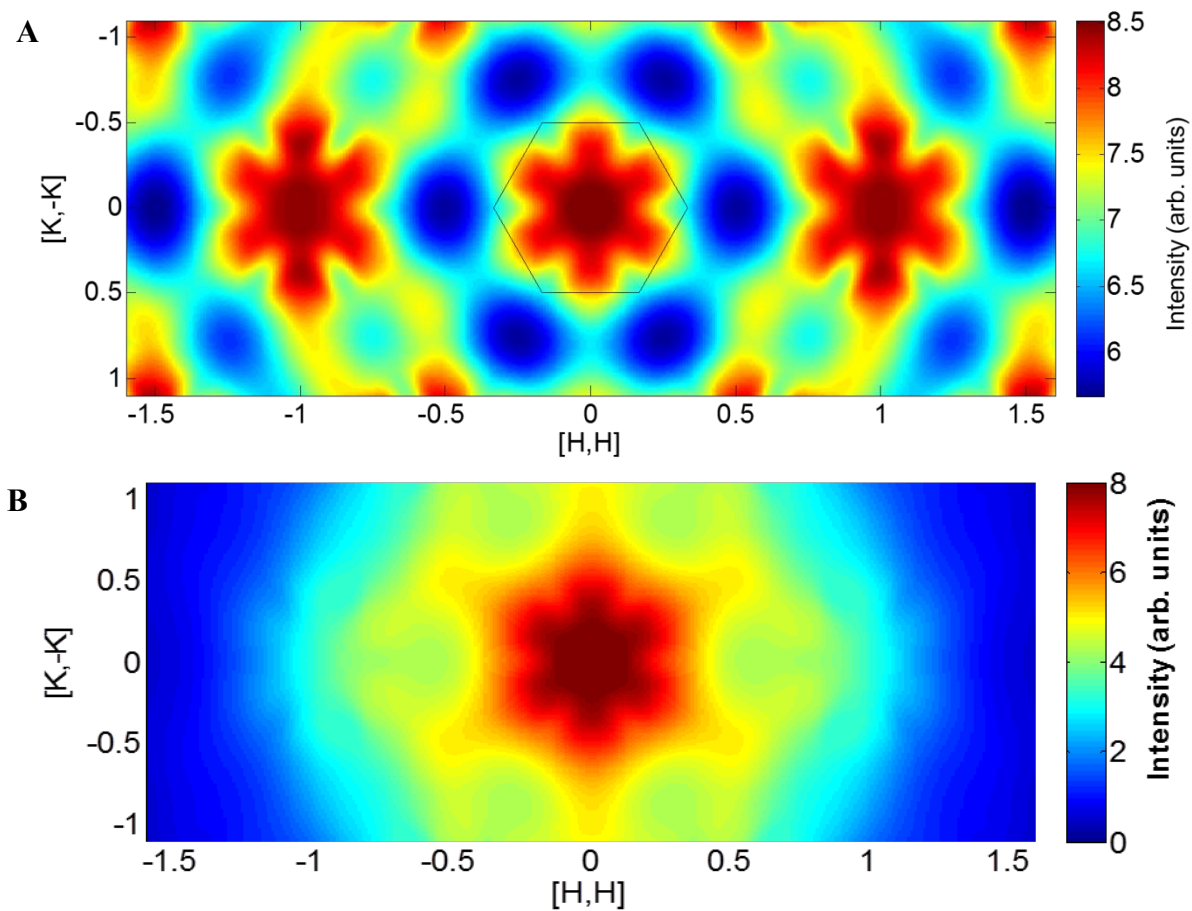


Fig. S10.

The results of the RPA calculation with $c_h = 0.35$ as described in main text (A) without and (B) with the Ru^{3+} form factor for $C_l = 1$.

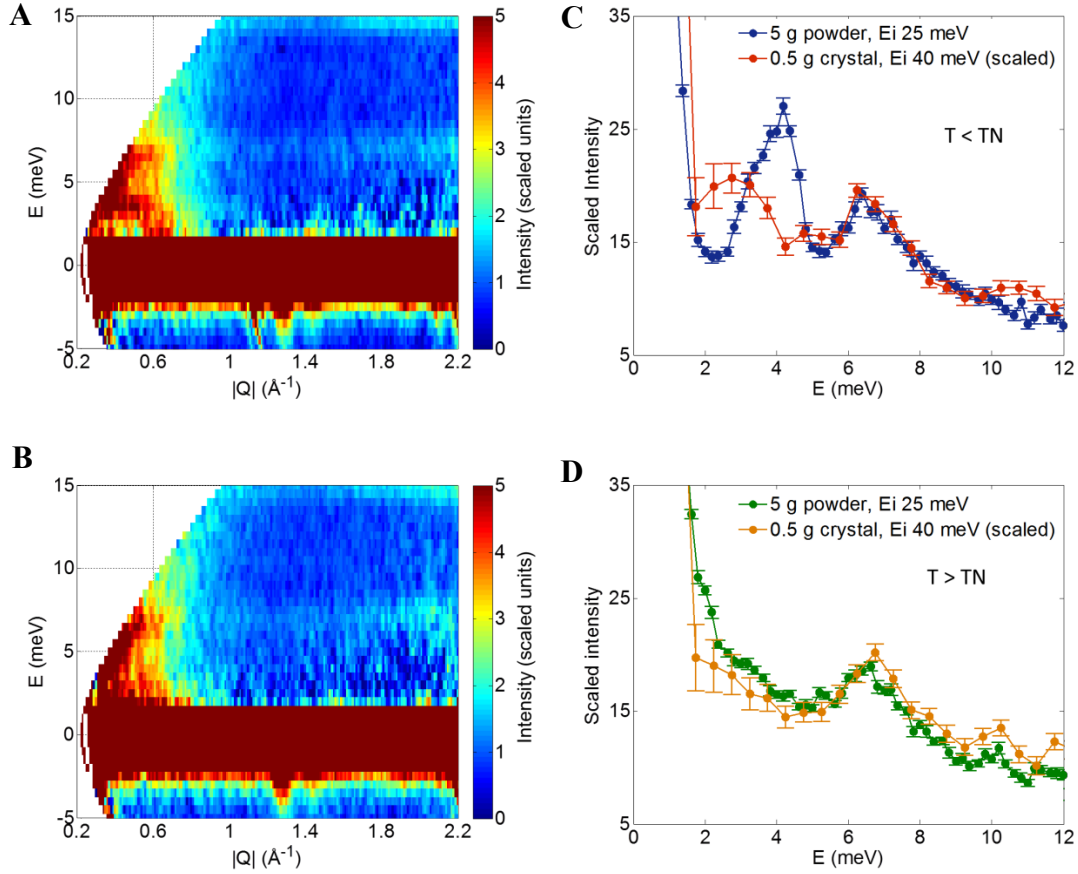


Fig. S11.

The pseudo ‘powder-averaged’ single-crystal data and comparisons to data from a true powder sample (25): (A) (B) Orientationally averaged, empty-cell background corrected, single-crystal data taken at SEQUOIA with $E_i = 40$ meV plotted as a function of $|Q|$; compare with Fig. 3 of reference (25). (A) $T = 5$ K, below T_N . (B) $T = 10$ K, above T_N . (C) The constant- Q cuts integrated over the range $Q = [0.5, 1.25]$ \AA^{-1} for data taken below T_N at $T = 5$ K. The single crystal data (red) was measured with $E_i = 40$ meV. The data from the powder (blue) was measured with $E_i = 25$ meV (25). Data are scaled to fit on the same plot. The broad ‘upper mode’ around 6.5 meV appears essentially identical in both samples. Differences in the scattering at low energies reflect differences in the spin wave spectra as discussed in the text. (D) The same comparison for the corresponding data for $T > T_N$ is presented for the pseudo-averaged single crystal data ($T = 10$ K, orange) and the powder data ($T = 15$ K, green) from ref. (25). The ‘upper mode’ feature is unchanged in both single crystal and powder, both below and above T_N . (Errorbars represent one standard deviation.)

Supplementary Table

T (K)	Component	A	E_0 (meV)	Γ (meV)
5				
	Continuum	5.5(1.4)	8.9(0.7)	13.5(1.8)
	Spin-wave 1	4.8(1.2)	3.28(0.09)	2.15(0.35)
	Spin-wave 2	0.45(0.18)	6.30(0.07)	0.91(0.31)
10	Continuum	13.2(3)	7.6(0.3)	15.2(1.2)
120	Continuum	3.7(0.1)	8.6(0.4)	12.7(1.3)
All temps	Background	1.0		

$$DHO(E, E_0, A, \Gamma, T) = \frac{2}{\pi} \times \frac{AE\Gamma E_0^2}{(E^2 - E_0^2)^2 + (E\Gamma)^2} \times \frac{1}{\left(1 - \exp\left(-\frac{E}{k_B T}\right)\right)}$$

Table S1.

This table shows the lineshape fit parameters for constant Q cuts describing the inelastic contributions to the scattering line-shapes for the energy cuts at the 2D zone center for temperatures of 5, 10 (Fig. 3A, B) and 120 K (Fig. S6D). The fits assumed that the elastic line is represented by a Gaussian with the FWHM equal to the calculated energy resolution. The background is assumed to be flat, with a value inferred from the negative energy transfer data at T=5 K. Note that the background level has a certain degree of systematic uncertainty depending on the negative energy cutoff used. The inelastic features are represented by DHO functions as shown in the tab below the table. The uncertainties (shown in brackets) are statistical only, and the parameters are strongly correlated with each other and with the chosen background. We do not necessarily attribute physical significance to the values or to their temperature dependence, but it is worth noting that the average characteristic energy E_0 of the continuum is 8.3 meV and the width parameter Γ is approximately 14 meV. The characteristic value E_0 occurs at a higher energy than the upper spin wave mode.